https://doi.org/10.1595/205651323X16848455435118

Johnson Matthey Technol. Rev., 2024, **68**, (1), 121–146

JOHNSON MATTHEY
TECHNOLOGY REVIEW

technology.matthey.com

Benchmarking Stability of Iridium Oxide in Acidic Media under Oxygen Evolution Conditions: A Review: Part I

Probing degradation of iridium-based oxide catalysts

James Murawski*, Soren B. Scott, Reshma Rao
Department of Materials, Imperial College London, Exhibition Road, London, SW7 2AZ, UK

Katie Rigg, Chris Zalitis, James Stevens, Jonathan Sharman
Johnson Matthey, Blount's Court, Sonning Common, Reading, RG4 9NH, UK

Gareth Hinds
National Physical Laboratory, Teddington, Middlesex, TW11 0LW, UK

Ifan E. L. Stephens
Department of Materials, Imperial College London, Exhibition Road, London, SW7 2AZ, UK

***Email:** j.murawski18@imperial.ac.uk

PEER REVIEWED

Received 10th February 2023; Revised 15th May 2023; Accepted 22nd May 2023; Online 23rd May 2023

State-of-the-art proton exchange membrane (PEM) electrolysers employ iridium-based catalysts to facilitate oxygen evolution at the anode. To enable scale-up of the technology to the terawatt level, further improvements in the iridium utilisation are needed, without incurring additional overpotential losses or reducing the device lifetime. The research community has only recently started to attempt systematic benchmarking of catalyst stability. Short term electrochemical methods alone are insufficient to predict catalyst degradation; they can both underestimate and overestimate catalyst durability. Complementary techniques, such as inductively coupled plasma-mass spectrometry (ICP-MS), are required to provide more reliable assessment of the amount of catalyst lost through dissolution. In Part I, we critically review the state of the art in probing degradation of iridium-based oxide catalysts.

1. Introduction

Hydrogen currently represents one of our most crucial chemical feedstocks with global annual production in excess of 90–120 million tonnes (1, 2), which is predicted to increase to over 660 million tonnes by 2050 (1). Its current principal use is in the synthesis of ammonia-based fertilisers *via* the Haber Bosch process. In principle, hydrogen can also be used as a replacement energy vector for fossil fuels, either electrochemically through the use of fuel cells to power vehicles, or *via* combustion of hydrogen, for example, in aircraft propulsion (3); for industrial processes such as steel production (4); and to help decarbonise heating of the home (5), such as the blending of hydrogen into the current gas network currently being trialled in the UK (6). Currently, 92–96% of the world's hydrogen is generated through non-renewable methods such as steam methane reforming (1, 7, 8), which utilises fossil fuels as a feedstock. In order to meet net zero targets, methods for the generation of terawatt levels of green hydrogen are required (9).

Green hydrogen describes hydrogen that is produced without the use of fossil fuels by electrochemical splitting of water, utilising renewable energy sources such as wind, solar and hydroelectric to provide the energy required. Currently, less than 8% of global hydrogen production comes from electrolysis, primarily alkaline electrolysis (7). Proton exchange membrane water electrolysers (PEMWEs) show great promise for generation of green hydrogen due to their high efficiency at high current density and fast start-up and shutdown capability (10), which make PEMWEs ideal for use alongside intermittent renewable energy sources. In addition, much of the knowledge and best practice established for PEM fuel cells can be translated to PEMWE technologies which can help accelerate their technological development (11). However, there is still room for further optimisation of system components specifically for PEMWE applications, including catalyst, membrane and catalyst layer deposition (12).

A large amount of research into PEMWE devices has focused on investigation of the anode catalyst, which is used to overcome the sluggish kinetics of the oxygen evolution reaction (OER). The most commonly studied catalysts are thermally prepared (13) IrO_x and RuO_x. The latter oxides are significantly less stable under typical PEMWE anode operating conditions (14–16), so this review focuses primarily on IrO_x. Iridium is one of the rarest elements found in the Earth's crust with annual production rarely exceeding 10 tonnes per year and industrial demand estimated to be around 7 tonnes in 2022 (17, 18). It is obtained as a byproduct of platinum mining and as such has a very inelastic supply (9), as iridium production can only be significantly increased by increasing platinum production which is unlikely to be increased solely based on iridium demand. The scarcity of iridium poses a significant, although not insurmountable, challenge for the terawatt level implementation of this technology (9) as at current loadings (2 $mg_{Ir}\ cm^{-2}$), 1 tonne of iridium would generate approximately 2 GW of PEM electrolyser capacity. Bernt *et al.*, estimated than in order to achieve terawatt (TW_{H2}) level PEMWE capacity, a reduction in loading of iridium in the anode catalyst or improvement of iridium utilisation by around 40 times (target: 0.05 $mg_{Ir}\ cm^{-2}$) is required, without compromising the performance or stability (19–21). While Clapp *et al.* (18) used industrial and academic iridium utilisation targets to model a realistic development profile towards 0.04 $mg_{Ir}\ W^{-1}$ in 2050, which corresponds to a lower loading limit of 0.10 $mg_{Ir}\ cm^{-2}$. They concluded that if these targets were achieved it would allow 1.3 TW_{H2} capacity using only 20% of the annual global primary iridium supply with a closed-loop iridium recycling program.

Current PEMWE systems are expected to provide >60,000 h of continuous operation (7). Assessing the performance and stability of anode catalysts represents a key challenge towards the improvement and scalability of PEMWE systems. Recently, more attention has been dedicated to identifying the limitations of testing anode catalyst lifetimes, the various artifacts that can occur during aqueous model testing and the experimental differences from real systems (22–25). The aim of this review is to outline the major artifacts that have impeded or continue to impede OER degradation testing, to present the different factors that affect catalyst degradation and how these relate to full cell testing, and to provide comments on some best practices for stability studies in general.

1.1 Comparison of Operating Conditions in Aqueous Model Systems and Full Cell Testing

The conditions the catalyst will be exposed to during constant operation, start-up, and shutdown in an electrolyser system are important when establishing criteria to benchmark potential new candidates for further OER testing. However, it is not usually practical to test a catalyst in a real electrolyser, where its performance is convoluted with that of other components. A test setup is often used in which the performance of the catalyst can be studied specifically and conveniently. Establishing the difference between the test setup and real application, and the effects that these differences will have on results is key to determining what is and isn't practical when trying to replicate PEMWE catalyst performance in smaller scale testing. Test systems lie on a spectrum from most fundamental to the most similar to the real system. The test system best approximating the 'real system' that will be analysed is the PEMWE catalyst-coated membrane (CCM) in a single cell membrane electrode assembly (MEA) setup (**Figure 1(a)**). A stack of these MEAs with associated water and power systems will form the basis of an operational system (**Figure 1(b)**).

Aqueous model systems (AMS) (22, 26) are cells that typically only investigate a single electrode material, usually the anode catalyst, and are used to simulate operation of that material in a simplified setup. The most common of these is the study of thin films of catalyst on a rotating disc electrode (RDE), **Figure 1(c)**, where mechanical

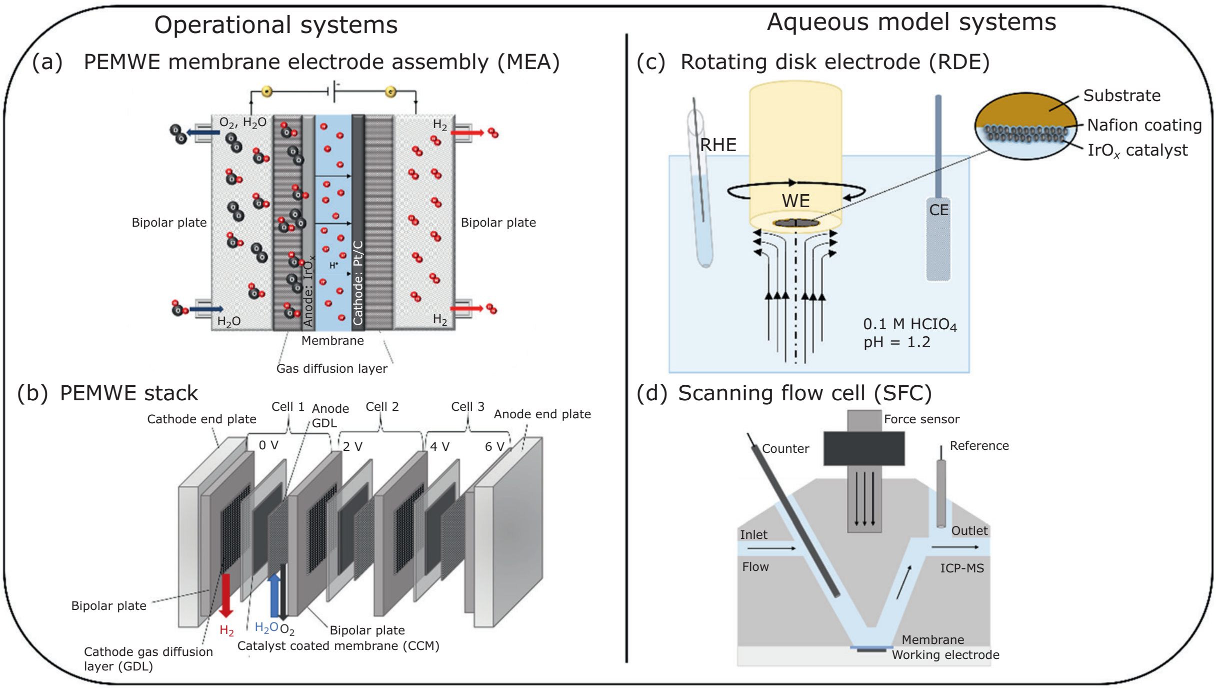

Fig. 1. Schematic of various operational systems: (a) diagram of PEMWE MEA; (b) simplified schematic of PEMWE stack consisting of multiple MEA cells and AMS; (c) RDE; (d) SFC, to illustrate some of the major differences in both reactant/product flow and electrode interface

cavitation helps with mass transport, for removal of formed oxygen bubbles. Alternately, scanning flow cells (SFCs), **Figure 1(d)** utilise a constant flow of liquid electrolyte allowing for constant sampling of the electrolyte with complementary techniques such as ICP-MS (27). A comparison of OER catalytic stability calculated from online SFCs showed that the calculated lifetime of the catalyst was often considerably less than that seen in a MEA, often by several orders of magnitude (28) for the same catalyst. This indicates that acidic aqueous setups such as SFC and RDE represent a considerably harsher environment, accelerating catalyst dissolution relative to real world conditions (see Section 3.3 for more details).

The primary physical differences are catalyst loading (RDE: 0.020 mg_{Ir} cm^{-2} *vs.* MEA: 2 mg_{Ir} cm^{-2}), temperature (RDE: room temperature *vs.* MEA: 60–80°C) and chemical environment (RDE: 0.1 M $HClO_4$ at pH 1.2 *vs.* MEA: deionised water (pH 7.0 with no dissolved ions, contact with air drops pH due to dissolved CO_2 from air turning it slightly acidic >pH 6)) and protons in perfluorosulfonic acid (PFSA) membrane. Further discussion on challenges of pH measurements in MEA systems are given in Section 3.3. Research has shown that cathode catalyst loading of MEAs can be reduced by up to an order of magnitude with no significant negative effect on performance (19); however, typical RDE model systems will still have a much lower geometric loading than the MEA. The method by which the catalyst layer is deposited also differs (29). For RDE this is typically done *via* drop casting while MEA CCM are usually prepared by a method of spray coating, k-bar/Meyer rod coating or decal transfer which utilises one of the previously mentioned techniques to create a layer onto polytetrafluoroethylene (PTFE) and transferring onto a membrane. Drop casting allows for accurate low mass loading to be obtained, although typically at the cost of layer homogeneity which can be a factor resulting in lack of reproducibility between samples of the same loading (30). Spray coating, which can be utilised for layer preparation of any system, typically is used for CCM preparation allowing for layers to be prepared with good layer homogeneity, although resolving the loading can be more challenging especially on low loading small surface area samples. A comparison between the conditions typically encountered in each type of test can be seen in **Table I**.

Table I Comparison of Typical Operating Conditions in Aqueous Model Testing and Full Cell Testing

Typical conditions	AMS, RDE	PEMWE system, MEA
Operational current density	10 mA cm^{-2}	2 A cm^{-2} @ 1.9 V (2022 DoE) (31); 3 A cm^{-2} @ 1.8 V (2030 DoE)
Operational potentials	1.2–1.7 V (2.0 V) (operation at higher potential limited by O_2 bubble formation)	Approx. <2 V cell voltage @ 2 A cm^{-2}, 1.6–1.65 V (32, 33) (accounting for *iR* drop)
Catalyst loading type	Deposited layer	CCM loading (7, 34)
Anode loading	IrO_x: 0.01–0.1 mg_{Ir} cm^{-2}	IrO_x: 2 mg_{Ir} cm^{-2}
Cathode loading	Pt/carbon counter	Pt/C: 0.3–0.5 mg_{Pt} cm^{-2}
Catalyst deposition method	Drop casting	Spray coating/decal coating/bar coating
Electrolyte	0.1 M $HClO_4$/0.05 M H_2SO_4 (Type 1 ultra-pure water)	PFSA membrane (i.e. Nafion®) with Type 1 ultra-pure water
Conditioning gas	Air/sat. Ar/sat. N_2	Anode sat. O_2 generated from operation
Pressure	Ambient pressure (1 bar)	≤30 bar
Acidic environment	1.2 pH (0.1 M $HClO_4$)/0.05 M H_2SO_4	pH measurement difficult but can be assumed to be in strongly acidic environment
Temperature standard (possible)	RT (operation at 60–80°C possible with limitations)	60–80°C (RT measurements possible but not typically done due to significantly lower performance)
Electrode setup	Three electrodes: working-anode catalyst (IrO_x), counter-cathode (Pt mesh), reference	Two electrodes measure overall cell voltage (reference electrode possible but not commonly used (33))
Test duration	0.5–48 h (35, 36)	100–4000 h (37, 38); expected lifetime: 7–10 years; >60,000 h operation (7)

1.2 PEMWE Catalyst Degradation Mechanisms

In a working PEMWE there are multiple effects that can lead to degradation of the catalyst performance. These include: passivation of the porous transport layer (PTL) which increases the contact resistance (39–41); poisoning of the anode or cathode catalyst which reduces activity or available surface area (38, 42); particle growth and restructuring (43); layer cracking; and catalyst detachment and dissolution (38). A simplified schematic of these processes can be seen in **Figure 2**. While understanding and mitigating against all these types of degradation is important for PEMWE development, the focus of this review is anode catalyst degradation and testing in AMS, so the primary degradation mechanisms of interest are dissolution and detachment.

While the mechanism for IrO_x catalyst dissolution under oxygen evolution conditions is still debated (44–46), catalyst loss in conventional RDE experiments, or any other method that utilises nanoparticle-based catalysts, can be split into several different pathways. The first is electrochemical dissolution where oxidation of IrO_x directly or indirectly results in the loss of iridium ions into aqueous solution. The second method is mechanical detachment or erosion of the nanoparticles from the electrode surface, which can be exacerbated by oxygen bubble formation at high current densities (24). Detachment can be a particular problem for RDE systems as unlike a PEMWE MEA, which has an optimised gas diffusion layer (GDL) to aid in the transport of the oxygen generated, the RDE is a flat planar surface. The use of PFSA ionomer such as Nafion® in the layer mitigates some of this detachment by acting as a binder, adhering the nanoparticle catalyst to the surface. Detachment in a MEA setup can occur in the form of layer cracking and loss of electrochemical contact. While detachment may be resolved by layer optimisation, the primary catalyst loss mechanism that cannot be easily mitigated is iridium dissolution. Unlike in an RDE or flow cell, where dissolved material is quickly carried away from the surface by the bulk electrolyte, dissolution in an MEA results either in redeposition on the anode catalyst, which should not result in activity loss, or deposition in the membrane or at the cathode catalyst (38).

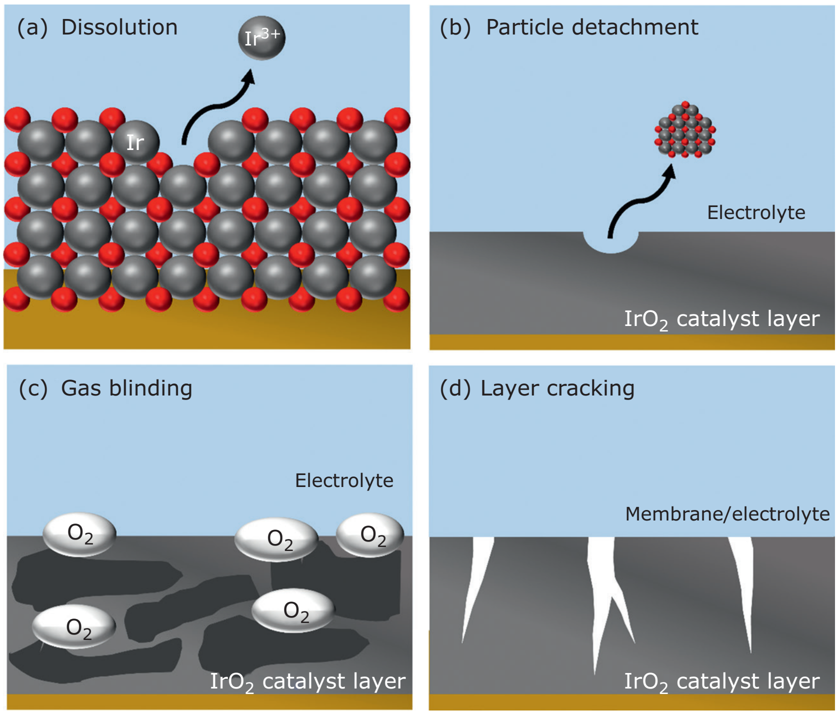

Fig. 2. Schematic showing different types of catalyst performance degradation including: (a) simplified schematic of iridium dissolution (for more detailed predicted mechanism see **Figure 4**); (b) particle detachment; (c) gas blinding or microporous layer blockage typically observed to a greater extent in low mass transport systems such as RDE; (d) layer cracking of deposited catalyst layer more generally seen in CCM testing due to the thicker nature of the catalyst layer

1.2.1 A Quick Primer on the Types of Iridium Oxide

When comparing iridium-based electrocatalysts, it is important to consider the different types of IrO_x and the effect the structure has on both its physical and electrochemical properties. Typically, iridium-based oxides are split into two major types: crystalline, typically characterised by a rutile IrO_2 phase; and amorphous, which usually has a more disordered higher surface area structure. The categorisation into crystalline and amorphous is made more complex when discussing iridium nanoparticle catalysts, which will often be composed of IrO_x units having either long or short-range order, with varying activity and stability. These two forms are not the only types, but they represent the most studied in the literature. Other forms of iridium-based catalysts include: molecular (47–49), perovskite (50, 51), hollandite (52) and pyrochlores (53–56). The other type worthy of mention is metallic iridium, sometimes referred to as iridium black, although the catalyst will undergo oxidation during operation at OER potentials to form a surface oxide and would generally be considered to be amorphous, in practice a variety of factors can affect the surface oxide layer that form (36).

Thermally prepared IrO_x are generally more stable than electrochemically prepared IrO_x nanoparticle catalysts toward the OER (13), with the difference being attributed to a more complete oxidation of the iridium to the more stable rutile IrO_2 form. Increasing crystallinity is shown to result in greater stability of the catalyst with respect to dissolution but tends to reduce activity (57, 58). Work by Abbott *et al.* (59) demonstrated that increasing the annealing temperature, used to synthesise a series of IrO_x nanoparticle catalysts, results in increasing crystallinity, determined by X-ray diffraction (XRD) and transmission electron microscopy (TEM) analysis. The catalysts annealed at higher temperature resulted in the formation of rod-shaped nanoparticles with an increased proportion of the 110 surface, alongside reduced Brunauer-Emmett-Teller (BET) surface area and a decreased intrinsic activity. In addition to this, the samples obtained from a lower annealing temperature were demonstrated to have iridium in a mix of the 3+ and 4+ oxidation states at 1 V_{RHE} that convert to the higher oxidation states on anodic polarisation (59, 60). Overall, the trend indicates hydrous IrO_x as being some of the more active but least stable catalysts and rutile IrO_2 as lower activity but most stable catalysts as demonstrated by Geiger *et al.* in **Figure 3** (28).

The fundamental reasons that crystalline OER catalysts are more stable than their amorphous counterparts is an area of ongoing research (28, 58, 61–63). Many of these studies employ

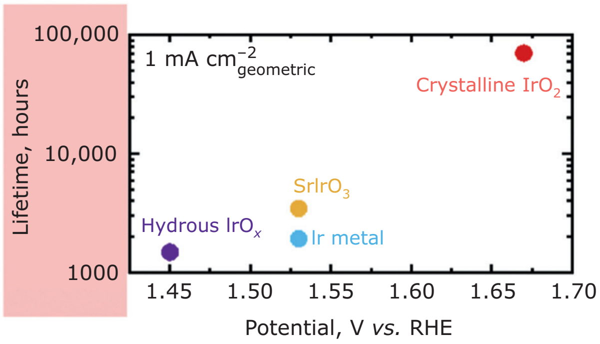

Fig. 3. Comparison of estimated lifetimes calculated from stability number *vs.* potential at 1 mA cm^{-2} current density in 0.1 M $HClO_4$ for various types of IrO_x catalysts. Data replotted from Geiger *et al.* (28)

isotope-labelling experiments, which indicate that the propensity to incorporate oxygen from the electrocatalyst into the oxygen evolved is, like activity, higher for less crystalline catalysts, though the importance of this correlation is debated (58). The electrochemically accessible surface area is higher for less crystalline materials (59, 64), but this cannot be the sole explanation because it would predict that dissolution rate and oxygen evolution rate are proportional across materials at a given potential, which is not the case (28, 58). A full discussion of these works is out of the scope of the present article, but future insights into the interplay of electrocatalytic and dissolution mechanisms would be useful for the wider OER research community.

This trend of the more active catalyst being less stable led to a proposed 'universal correlation' between activity and corrosion susceptibility of OER catalysts and various thermodynamic explanations for this correlation (65). While an inverse relation between activity and stability is seen in some nanoparticle studies (59), particularly with the increasing crystallinity with temperature of synthesis, it is not universal when looking at the relative stability of specifically orientated RuO_2 single crystal surfaces (66). Work by Roy *et al.* showed there was no correlation between the most active and most stable RuO_2 surface orientation, and that higher dissolution rates may be a result of less stable defect sites (66). Whilst the effects of specific crystal orientation of IrO_2 have been investigated for activity (67–69), there are limited studies that investigate stability of different IrO_2 crystallographic orientations (68). Work by Scohy *et al.* indicate that there is a convergence in activity and stability between IrO_2 catalyst surfaces with different initial crystallographic orientation (hkl) after a period of conditioning and operation (68). Indicating that tuning of the operational surface is of greater importance than the initial surface state. Further systematic studies on different crystallographic orientations of IrO_2 such as those that have been conducted on RuO_2 (66) could prove valuable in confirming the most beneficial surfaces both for activity and stability during operation to help inform future nanoparticle catalyst design.

1.2.2 Mechanism of Iridium Dissolution

Recently, the focus of the electrocatalysis community has been shifting from activity to stability in fundamental studies of the OER (70). Computational approaches have mostly relied on thermodynamics. The electrochemical reactions included in the Pourbaix diagram for iridium (71) are:

$$Ir \rightleftharpoons Ir^{3+} + 3e^- \quad E = 1.156\ V + 0.0197 \log (Ir^{3+})\ V \tag{i}$$

$$Ir^{3+} + 2H_2O \rightleftharpoons IrO_2 + 4H^+ + e^- \quad E = 0.233\ V - 0.2364pH - 0.0591 \log (Ir^{3+})\ V \tag{ii}$$

$$IrO_2 + 2H_2O \rightleftharpoons IrO_4^{2-} + 4H^+ + 2e^- \quad E = 2.057\ V - 0.1182pH + 0.0295 \log (IrO_4^{2-})\ V \tag{iii}$$

An estimate of the stability with respect to these reactions, which can be extended to ternary oxides, is the Gibbs Pourbaix decomposition reaction, which has been proposed as a metric on which to screen for novel OER catalysts (72).

Experimentally, mechanistic studies of dissolution have been based on comparing ICP-MS measurements of iridium dissolved in the electrolyte with activity measured by electrochemistry, often coupled with mass spectrometry and isotope labelling (15, 28, 46, 58, 73). Kasian *et al.* proposed a mechanistic picture combining dissolution pathways with the oxygen evolution catalytic cycle, shown in **Figure 4**. This includes the three reactions covered by Pourbaix: dissolution of iridium as Ir^{3+} (Equation (i) above) with IrO_2 to Ir^{3+} (Equation (ii), *via* IrO_2OH and oxygen release as O_2) and IrO_2 to IrO_4^{2-} (Equation (iii), *via* IrO_3). The view is based on experimental evidence for two pathways with distinct potential dependence: one is proposed to occur at lower overpotential *via* $HIrO_2$ and another at higher overpotential *via* IrO_3. The high overpotential pathway proceeds

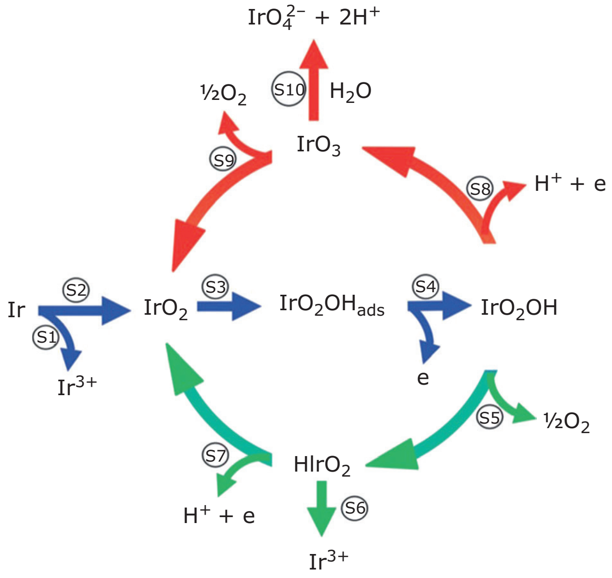

Fig. 4. Two proposed pathways for iridium dissolution. In green is low overpotential pathway. Red is the high overpotential pathway *via* IrO_3 intermediate. Reproduced from Kasian *et al.* (46) under CC-BY-NC license

via the formation of IrO_3 intermediate, which can be in a gaseous form as qualitatively detected by differential electrochemical mass spectrometry (DEMS) (46).

Consistent with these proposed mechanisms, a recent kinetics-based computational study (74) indicated that iridium dissolution from IrO_2 (110) can proceed *via* oxidation of oxo adsorbed sites (IrO_3) to IrO_4^{2-}. Later works utilising chip electrochemical mass spectrometry (EC-MS) confirmed links between lattice oxygen release and dissolution in IrO_x and RuO_x, also previously observed (15) results that a large portion of dissolution occurs during the ramp-up period (58). Much more work remains to be done to understand the mechanisms and descriptors of dissolution to enable design of more stable OER catalysts.

1.3 Definitions of Stability

A stable PEMWE oxygen evolution catalyst should withstand the acidic environment, temperature and applied potential without a loss in anode catalyst activation overpotential. Accurate determination of these parameters is essential for conducting testing of catalyst stability outside of operational systems. The local potential experienced at the catalyst surface is approximately ≥ 1.6–1.65 V_{RHE} after accounting for ohmic (*iR*) drop (32, 33) in MEA testing. A commercial electrolyser system is expected to last at least 7–10 years (7, 75), but testing on this timescale is usually not practical, especially when testing new catalysts. In this case, accelerated test methods that predict catalyst lifetime under operational conditions are required. Techniques used to evaluate stability are tabulated in **Table II**, and metrics providing quantitative definitions of stability measurable by these techniques are tabulated in **Table III**.

ICP-MS techniques have been used to benchmark different catalysts by comparing their stability number (S-number) a proposed metric (28) derived from the ratio of oxygen production rate (determined from the current) to iridium dissolution rate (detected by ICP-MS). **Table IV** shows a comparison of the stability and activity of different OER catalysts *via* the S-number metric: it indicates that the higher surface area rutile type IrO_x catalysts demonstrate the highest ratio of oxygen evolved to dissolved iridium, indicating their suitability for further testing at the MEA level.

2. Overview of Stability Studies

2.1 Aqueous Model Systems

Most reports of stability of oxygen evolution catalysts rely entirely upon the use of electrochemical tests for predicting catalyst lifetime. A common version of this technique is constant operation in an AMS at a given current density (for example, 10 mA cm^{-2}) with measurement of the change in overpotential over the course of 0.5–48 h (97–101). This constant current operation is seemingly comparable to the operation of a real hydrogen producing electrolyser, when loading is scaled (~100 times reduction in loading 2 mg cm^{-2} *vs.* 10–20 μg cm^{-2} and ~100 times reduction in current density 1–2 A cm^{-2} *vs.* 10 mA cm^{-2}). However, there have always been issues with assessing stability through constant current experiments in model setups. Firstly, the time frame is insignificant in comparison to the lifetime of an electrolyser (0.5–48 h *vs.* 5+ years). Secondly, when conducted for periods in the region of 24 h a large shift in overpotential can occur (84). The increase potential can be due to several different factors (116) which are split into catalyst degradation (catalyst passivation, detachment, agglomeration and dissolution) and experimental artifacts (gas blinding of the catalyst surface and support passivation). Overall, this makes it difficult to resolve any degradation process that is occurring by use of electrochemical measurements alone. Finally, there is a question about whether

Table II Overview of Techniques for Assessing Catalyst Stability

Technique	Description	Advantages	Limitations	Ref.
Electrochemical setup				
Membrane electrode assembly (MEA) (76)	Typically consists of a CCM sandwiched between GDL with a flow field on either side	More comparable to real systems because it utilises a CCM; high current density operation >1 A cm^{-2}	Increasing cell complexity; can be difficult to deconvolute anode catalyst performance from other cell processes/ losses; typically, higher loading and larger quantity of material required per test	(22, 32, 36, 38, 77–79)
Rotating disk electrode (RDE) (80)	Planar electrode (disc insert) that is rotated resulting in laminar flow to the electrode surface, primarily used in an aqueous three-electrode setup	Commonly available method; can operate with low catalyst loading	Reproducibility issues due to drop casting catalyst layers on disc inserts; O_2 gas blinding issues; not representative of MEA operation	(24, 35, 81)
Rotating ring disk electrode (RRDE) (80)	The same setup as a RDE with the addition of a second working electrode in the form of a ring around the disc allowing for monitoring of products formed at the primary working electrode *via* observed electrochemistry	Capable of monitoring products generated at the main working electrode if they can be monitored through an electrochemical process (for example redeposition of a dissolved metal ion)	Existing issues with RDE; added complexity and requirements (bipotentiostat, 2 channels); ring measurements can only distinguish to approx. 1% Faradaic efficiency; does not specifically identify the species	(82, 83)
Modified rotating disk electrode (MRDE) (84)	Recently proposed setup utilising RDE structure and aqueous cell but incorporating small CCM working and counter electrode section	Possible to obtain very high current density i.e. 3 A cm^{-2}; uses CCM that is comparable to commercial setup	Early stage of utilisation; manufacture of CCM is required, increasing sample complexity	(84, 85)
Scanning flow cell (SFC) (27)	Stationary working electrode with a flow of electrolyte across the working electrode with the counter electrode placed slightly upstream and reference electrode slightly downstream	Can more easily be coupled with online detection techniques such as ICP-MS due to constant flow of electrolyte	Complex setup; small timescales; stationary electrode typically with no GDL limiting upper potential and catalyst loading	(16, 86–88)
Gas diffusion electrode (GDE): floating electrode (89), GDE setup (90, 91)	Working electrode incorporates some more advanced methods of GDL allowing for flow of reaction product gases away from the electrode	High mass transport utilised previously for ORR studies (89). Preliminary studies indicate this could be transferable to OER for increased removal of O_2	Early stages of optimisation for use with OER; stationary electrode (no mechanical bubble removal either through rotation or flow)	
Complementary Techniques				
Inductively coupled plasma-mass spectrometry (ICP-MS)	Detection of dissolved/ solution catalyst species (Ir, Ru etc.) in electrolyte using quadrupole mass spectrometry to obtain quantified dissolution rate	Very high sensitivity especially to elements like Ir which are not commonly occurring; typical lower detection limit ~0.1 ppb; online capability with SFC	Sensitive technique requires high degree of maintenance to ensure reliable operation and measurements; high operational costs	(35, 92); SFC; (16, 86–88)

Table II Continued

Technique	Description	Advantages	Limitations	Ref.
Complementary Techniques (Continued)				
Electrochemical quartz crystal microbalance (EQCM) (93)	Highly sensitive mass balance functions as the working electrode in an aqueous three-electrode setup allowing for monitoring of mass loss	Capable of observing all mass loss including detachment and dissolution; *In situ* technique allows for tracking alongside electrochemistry	Can't distinguish between mass loss from detachment and dissolution; Mass gain is also possible due to oxide formation can complicate study	(92, 94)
Electrochemical mass spectrometry (EC-MS): DEMS, OLEMS (27), and chip EC-MS (95)	While process varies between different techniques all involve connecting an electrochemical cell to some form of mass spectrometer to monitor primarily gas phase reaction/dissolution products (O_2, IrO_3 etc.)	Has been used to detect intermediate species of some dissolution processes (46); can utilise labelled oxygen for fundamental studies (58)	Limited time response; typically, only semi-quantitative (with the exception of chip EC-MS (95))	(46, 61)
Identical location transmission electron microscopy (IL-TEM)	High magnification electron microscopy imaging of the same region of catalyst that is measured before and after testing to observe degradation and shape change in the nanoparticles	Can directly observe changes in morphology of individual and groups of particles with cycling and operation	Catalyst support often required to disperse particles, instability of support results in large amount of degradation as a result of support degradation; specific TEM substrate required to enable identical location observations	(60, 96)

Table III Overview of Stability Metrics

Metric	Equation	Measured	Scale (AMS/ MEA)	Advantages	Limitations	Ref.
Constant current, change in voltage over time (97)	U (t1)–U (t0)	Chronopotentiometry (2 h, 24 h) @10 mA cm^{-2}; typical loading: 0.01–0.1 mg cm^{-2}	AMS/ MEA	Simple; can be combined with *ex situ* characterisation techniques	Gas blinding of surface leads to eventual cascading increase in potential (may be mitigated by GDE); does not provide information on origin of instability; loading and layer dependant	(97–101)
Constant potential, change in current over time	I (t1)/I (t0)	Chronoamperometry (0.5–48 hr) @1.6–1.8 V (1.65 V_{RHE})	AMS/ MEA	Simple; potential control ensures the same driving force for electrochemical dissolution allowing for easier observation of intrinsic stability of a catalyst; can be combined with *ex situ* characterisation techniques	Gas blinding of surface leads to slow degradation of cell performance; does not provide information on origin of instability	

Table III Continued

Metric	Equation	Measured	Scale (AMS/ MEA)	Advantages	Limitations	Ref.
Accelerated stress testing (AST)/potential cycling, performance before and after cycling	I_{max} (cycle n)/I_{max} (cycle 1)	Current density *via* CV, CA and CP before and after either repeated CV or stepping potential into a region where there is OER (>1.5–1.65 V_{RHE}) and a region below (<1.2–1.4 V_{RHE})	AMS/ MEA	Short in comparison to long term (1000 h+) testing; capable of simulating repeated on/off cycles; demonstrated as being more stressful on some Ir-based catalysts; more representative of real-life operation with intermittent power supply	Needs to be coupled with other performance testing, e.g. constant current/ potential before and after cycling	AMS: (35, 96, 102, 103); MEA: (22, 35, 37, 43, 104)
Faradaic efficiency (105)	J_{O2}/J_{total}	Measuring the proportion of current density that goes toward oxygen evolution or dissolution	AMS	Can screen catalysts that have large proportion of current density going to non OER processes; mass spectrometry techniques could more accurately determine O_2 output at low current densities (58, 95)	Limited to stability studies of catalysts that are considered quite unstable (i.e. Ru based oxides) as Faradaic efficiency of stable catalyst to OER would be too close to 100% to observe any difference	
Stability number (S-number) (28)	n_{O2}/n_{diss}	Utilises constant current/potential measurement coupled with dissolution measurement; S-number = evolved oxygen (calculated from the current)/ dissolved Ir (calculated from ICP-MS)	AMS/ MEA	Can be utilised for both shorter and longer term measurements; independent of loading and the amount of active sites or surface area	Reliability of measurement is ultimately determined by dissolved Ir that is detected *via* ICP-MS	(28, 58, 106, 107)
Electrochemical surface area (ESCA) loss (108)	d (log (SA))/dt	Double layer capacitance/ capacitive area (108); absorption capacitance (EIS) (109)	AMS	Can be conducted alongside electrochemical testing in the same setup and conditions	High degree of uncertainty around techniques used for ECSA measurements of metal oxides; surface area can change for a variety of reasons including dissolution, detachment and catalyst restructuring	
Dissolution rate (27)	d (n_{diss})/ dt	Dissolution rate over a given time period at a specific current density or potential using *ex situ*/*in situ* ICP-MS	AMS/ MEA	Can monitor amount of Ir dissolved and monitor change with time to see effects of cycling/start-stop sequences	Online ICP-MS measurements required for short term experiments not widely available	
Mass loss (92)	d (m)/dt	Change in mass as measured with techniques such as EQCM	AMS	Direct observation of all changes, both detachment and dissolution	Mass loss can come from a variety of processes not all as relevant for catalyst stability studies (92); mass can also increase due to oxide formation etc.	

Table IV S-Number (Steady State /Transient) of Various Iridium-Based Catalysts[a]

Catalyst	Ir (Ru) stability		Lattice O_2 stability		Conditions	Ref.
	Steady state	Transient	Steady state	Transient		
Unsupported						
$Ir_{0.5}Ti_{0.5}O_x$	1.50×10^6	–	–	–	0.1 M $HClO_4$, 5 min, 1 mA cm^{-2}	(110)
$Ir_{0.7}Ru_{0.3}O_2$ b	1.00×10^6 (Ir); 1.00×10^5 (Ru)	–	–	–	0.1 M $HClO_4$, 1 min, 1 mA cm^{-2}	(111, 112)
IrO_2	9.20×10^5	–	–	–	0.1 M $HClO_4$, 10 min, 1 mA cm^{-2}	(110)
Porous IrO_x, 450°C	3.21×10^5	–	–	–	0.05 M H_2SO_4, 10 mA cm^{-2}, 80°C	(106)
IrO_x Alfa Aesar	2.17×10^5	–	–	–	0.1 M $HClO_4$, 1.7 V_{RHE}, GC substrate	(107)
$Ir_{0.7}Sn_{0.3}O_x$	1.60×10^5 (Ir); 5.00×10^4 (Sn)	–	–	–	0.1 M $HClO_4$, 5 min, 1 mA cm^{-2}	(112, 113)
$H_{3.6}IrO_43.7H_2O$ (Sr_2IrO_4)	1.50×10^5	–	–	–	0.1 M $HClO_4$, 1 mA cm^{-2}, 60 mins	(114)
$H_{3.5}IrO_4$	1.30×10^5	–	–	–	0.1 M $HClO_4$, 1 mA cm^{-2}, 60 mins	(114)
IrO_2 Sigma Aldrich	1.09×10^5	–	–	–	0.1 M $HClO_4$, 10 mA cm^{-2}, 180 mins	(102)
Ir metal	1.00×10^5	–	–	–	0.1 M HClO4, 5 min, 1 mA cm^{-2}	(110)
$SrCo_{0.9}Ir_{0.1}O_{3-\delta}$	8.05×10^4	9×10^2	–	–	0.1 M $HClO_4$, 10 mA cm^{-2}, steady state 180 mins, transient <60 mins	(102)
$SrIrO_3$, thin film	8.00×10^4	–	–	–	0.1 M $HClO_4$, 10 min, 1 mA cm^{-2}	(110)
Porous IrO_x, 500°C	6.99×10^4	–	–	–	0.05 M H_2SO_4, 10 mA cm^{-2}, 80°C	(106)
IrO_2 sputtered, 400°C	5.61×10^4	3.31×10^4	1.95×10^4	1.55×10^4	0.1 M $HClO_4$, 0.5 mA cm^{-2}, steady state 30 min, transient <2min	(58)
Ir metal	5.23×10^4	6.6×10^3	–	–	0.1 M $HClO_4$, 10 mA cm^{-2}, steady state 180 mins, transient <60 mins	(102)
IrO_2 comm.	5.12×10^4	–	–	–	0.05 M H_2SO_4, 10 mA cm^{-2}, 80°C	(106)
IrO_x, amorphous	5.00×10^4	–	–	–	0.1 M $HClO_4$, 5 min, 1 mA cm^{-2}	(110)
IrO_2 comm., 450°C	4.18×10^4	–	–	–	0.05 M H_2SO_4, 10 mA cm^{-2}, 80°C	(106)
6H-$SrIrO_3$	2.23×10^4	–	–	–	0.1 M $HClO_4$, 1 mA cm^{-2}, 60 mins	(114)
IrO_x sputtered, 25°C	1.51×10^4	1.2×10^3	1.07×10^4	4.1×10^3	0.1 M $HClO_4$, 0.5 mA cm^{-2}, steady state 30 min, transient <2min	(58)
IrO_x/Ir	9.1×10^3	7×10^2	3.5×10^3	8×10^2	0.1 M $HClO_4$, 0.5 mA cm^{-2}, steady state 30 min, transient <2min	(58)
Porous IrO_x–800°C	3.0×10^3	–	–	–	0.05 M H_2SO_4, 10 mA cm^{-2}, 80°C	(106)
$IrO_x.yH_2O$, E-chem cycled	2.0×10^3	2.5×10^2	2.4×10^3	5×10^2	0.1 M $HClO_4$, 0.5 mA cm^{-2}, steady state 30 min, transient <2 min	(58)

Table IV Continued

Catalyst	Ir (Ru) stability		Lattice O_2 stability		Conditions	Ref.
	Steady state	Transient	Steady state	Transient		
Unsupported (Continued)						
$Sr_2Ir_{0.5}Fe_{0.5}O_4$	2.0×10^3	–	–	–	0.1 M $HClO_4$, 1 mA cm^{-2}	(115)
IrO_2 comm., 800°C	1.6×10^3	–	–	–	0.05 M H_2SO_4, 10 mA cm^{-2}, 80°C	(106)
Porous IrO_x, 400°C	3×10^2	–	–	–	0.05 M H_2SO_4, 10 mA cm^{-2}, 80°C	(106)
RuO_2 sputter deposited	120	90	9.0×10^3	1.41×10^4	0.1 M $HClO_4$, 0.5 mA cm^{-2}, steady state 30 min, transient <2 min	(58)
RuO_x/Ru, E-chem oxidised	120	50	5.9×10^3	1.6×10^3	0.1 M $HClO_4$, 0.5 mA cm^{-2}, steady state 30 min, transient <2 min	(58)
RuO_x/Ru foam	100	7	2.25×10^4	1.4×10^3	0.1 M $HClO_4$, 0.5 mA cm^{-2}, steady state 30 min, transient <2 min	(58)
RuO_x sputter deposited	90	12	2.2×10^3	7×10^2	0.1 M $HClO_4$, 0.5 mA cm^{-2}, steady state 30 min, transient <2min	(58)
RuO_x/Ru E-chem oxidised after AST	–	55	–	1.5×10^3	0.1 M $HClO_4$, 0.5 mA cm^{-2}, transient <2min	(58)
Supported						
IrO_x/IrO_2 comm.	5.97×10^4	–	–	–	0.05 M H_2SO_4, 10 mA cm^{-2}, 80°C	(106)
IrO_x/TaTO-5-AG	3.51×10^4	–	–	–	0.05 M H_2SO_4, 10 mA cm^{-2}, 80°C	(106)
IrO_x/TaTO-2.5-AG	2.51×10^4	–	–	–	0.05 M H_2SO_4, 10 mA cm^{-2}, 80°C	(106)
IrO_x/C, 450°C	2.46×10^4	–	–	–	0.05 M H_2SO_4, 10 mA cm^{-2}, 80°C	(106)
IrO_2@TiO_2 NPs	1.00×10^4	–	–	–	0.1 M $HClO_4$, 5 min, 100 mA mg^{-1}	(110)
IrO_x/ATO-10-NFs	5.80×10^3	–	–	–	0.05 M H_2SO_4, 10 mA cm^{-2}, 80°C	(106)
IrO_x/C	3.9×10^3	–	–	–	0.05 M H_2SO_4, 10 mA cm^{-2}, 80°C	(106)
Ir/C comm.	3.4×10^3	–	–	–	0.05 M H_2SO_4, 10 mA cm^{-2}, 80°C	(106)
IrO_x/ATO-10-AG	3.3×10^3	–	–	–	0.05 M H_2SO_4, 10 mA cm^{-2}, 80°C	(106)
IrO_x/TaTO-18-AG	2.4×10^3	–	–	–	0.05 M H_2SO_4, 10 mA cm^{-2}, 80°C	(106)
IrO_x/C, 600°C	9×10^2	–	–	–	0.05 M H_2SO_4, 10 mA cm^{-2}, 80°C	(106)
MEA comparison, Alfa Aesar IrO_x						
MEA deionised water	4.52×10^7	–	–	–	Deionised water, 120 mins, 2 A cm^{-2}, ~55–60°C	(22)
MEA 0.1 M H_2SO_4	4.94×10^5	–	–	–	0.1 M H_2SO_4, 120 mins, 2 A cm^{-2}, ~55–60°C	(22)
Aqueous model system (AMS)	6.00×10^4	–	–	–	0.1 M H_2SO_4	(22)

[a] S-number ratio of activity to Ir dissolved given to closest 100, can be assumed to be conducted at room temperature unless otherwise stated. Transient time period varies between studies (see conditions)

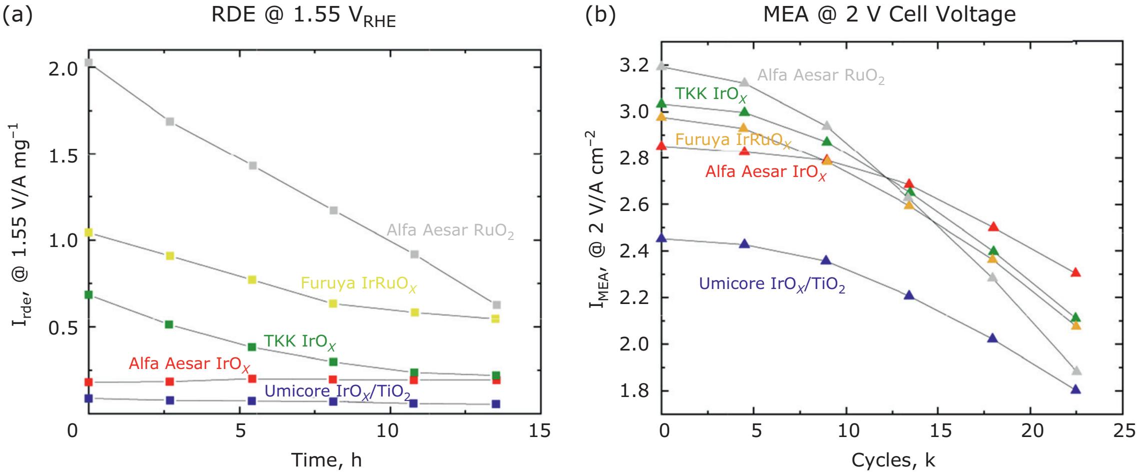

Fig. 5. (a) Degradation of current performance for several commercially available catalysts in a RDE system @ 1.55 V *vs*. RHE; (b) degradation of current performance of the same commercially available catalysts in a MEA cell square wave cycling between 1.45 V and 2 V holding for 30 s at each point. Data replotted from S. Alia *et al.* (36)

the overall anode catalyst trends observed in AMS studies are the same as those observed in MEA studies, as while activity studies typical show similar trends between the two systems (117, 118) some discrepancy has been observed in stability trends (36), see **Figure 5**.

2.1.1 Accelerated Stress Testing

As an alternative to constant current experiments, that can be hampered by rapid overpotential increases due to surface site blockage (25) or in the absence of high sensitivity online ICP-MS, accelerated stress testing (AST) can serve as another method by which to benchmark candidate OER catalysts. Potential cycling, such as that experienced during start-up and shutdown, has been shown with some catalysts to cause greater degradation than during constant operation (87). As a result, AST often takes the form of repeated potential cycling (triangle wave) or stepping between an overpotential (square wave) where there is activity (>1.6 V_{RHE}) and one where there is not (<1.3 V_{RHE}) in order to degrade the catalysts in conditions that could be equated to the operational region in a practical system such as in an electrolyser, where the ability to shut down and start up in a speedy manner is considered an advantageous trait. Extended cycling is not a new technique, with various iterations having been used previously to demonstrate the stability of catalysts outside of OER. The application of the technique can vary quite drastically: from 100–1000 cycles that demonstrate only short term cycle stability; to more robust accelerated degradation studies of 10,000 cycles (102), 15,000 cycles (103), 30,000 cycles (35) and 50,000 cycles (96) that vary in upper and lower potential limits alongside coupling with dissolution measurements.

A comprehensive empirical study using AST in a RDE AMS conducted by Alia *et al.* (35) investigated several test parameters such as upper potential cycle limit and hold *vs.* cycling as well as comparisons of low loading MEA in order to suggest initial best practices for OER catalyst testing. The findings indicated that there are limited ways to increase dissolution, with the upper potential limit demonstrating increasing, but limited, effect on dissolution of IrO_x catalysts. This is consistent with other results which show that after a higher initial dissolution rate there is limited effect of increasing the upper potential limit on overall dissolution (15), unless significantly higher potentials than would be expected (>1.8 V_{RHE}) in a operational PEMWE system are applied (35). The difference between potential holds and cycling is also of interest with Alia *et al.* indicating that there was limited difference, or even a slight increased degradation from the extended hold operation, where extended holds were conducted at various potentials for 13.5 h and cycling consisted of 30k cycles between 1.4 V and various upper limits with a varying scan rate to last for the same period of time. This contradicts the results shown in short timescale measurements that dissolution is highly dependent on the ramp up/down cycle as opposed to constant operation for iridium-based catalysts (15, 58) as well as the more generally held theory that potential cycling is a method for accelerating catalyst degradation (103).

There are several possible explanations for the discrepancy between the work of Alia *et al.* and others (103): (i) there is increased catalyst loss initially of particularly unstable parts of the catalyst (58); (ii) gas blinding of the catalyst layer prevents catalyst dissolution (24, 25, 85, 119); (iii) the ramp up/down dissolution increase is more dependent on what potential region of operation is used, specifically the lower potential limit (120), with the potential in the Alia *et al.* work not dropping below 1.4 V_{RHE}. While the idea that some catalysts might exhibit high initial dissolution before the rate slows down it is still worth considering from a screening perspective, it is likely that the lower potential limit is playing a greater role. In other works, both AST and short-term measurements are typically conducted over the broader 0.6–1.7 V_{RHE} range *vs.* 1.4 V_{RHE} to various upper potential limits conducted by Alia *et al*. By going significantly below 1.4 V_{RHE} there is the possibility of considerable change in the oxide catalyst *via* reduction which could aid in increased dissolution especially during repeated cycling experiments.

Irrespective of the cause of increased degradation, further investigation building on existing protocols would help not only with determining optimal conditions for screening but also will add understanding to the significantly reduced dissolution relative to activity over operation lifetime as seen in MEA studies (22). Questions also remain about the time dependency of performance testing, especially with CCM testing, with results from Papakonstantinou *et al.* (121) showing that catalyst changes from cyclic voltammetry (CV) (0.5–1.4 V) conducted after 7 mins and 18 h hold at 0.315 A cm^{-2}. Other research has noted that it can take up to 1000 h for CCM performance to stabilise (37). Indicating that it is possible that transient cycling may not be able to capture this reformatting phenomenon and instead be observing a less stable transient catalyst state.

2.1.2 Surface Blockage

El-Sayed *et al.* (25) observed a large increase in overpotential due to loss of catalyst surface area during constant current operation utilising a RDE setup and determined that it was not due to loss of catalyst through dissolution, but instead through gas blinding. This is where parts of the catalyst surface are blocked by oxygen trapped in the porous layer or particle pores. This leads to loss of the contact of most of the catalyst surface area with the electrolyte. When conducting constant current experiments a slow increase in voltage is observed until a cascading effect results in the overpotential increasing rapidly after a certain amount of time. An increased potential is applied to a smaller area increasing the dissolution that occurs as seen in **Figure 6(b)–6(d)**. The overpotential continues to increase until it reaches a plateau, which is at the same potential as the baseline measurement of OER on a gold-only disc as seen in **Figure 6(e)**, indicating that no active catalyst remains after this point either due to dissolution, detachment or blockage. The time length for rapid increase from experiment start is inversely proportional to the current density applied, further indicating that oxygen blocking the surface is the primary contributing factor.

The source of the overpotential increase was further identified by studies in a RDE setup that also utilised an ultrasonic horn, see

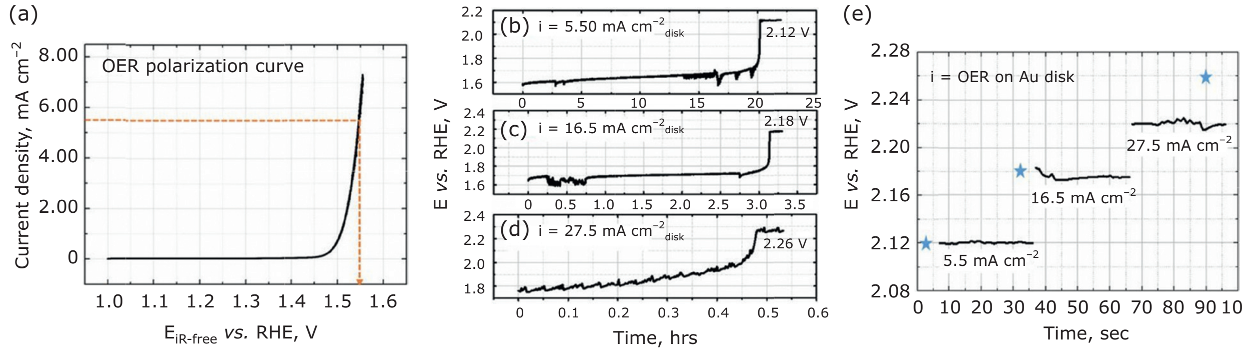

Fig. 6. (a) Deposited IrO_x catalyst layers on an Au disc insert; (b) IrO_x on Au plateau @ 20 h; (c) IrO_x on Au plateau @ 3 h; (d) IrO_x on Au plateau @ 0.45 h; (e) blank Au disc insert baseline reading. Reproduced from El-Sayed *et al.* (25), under CC-BY 4.0 license

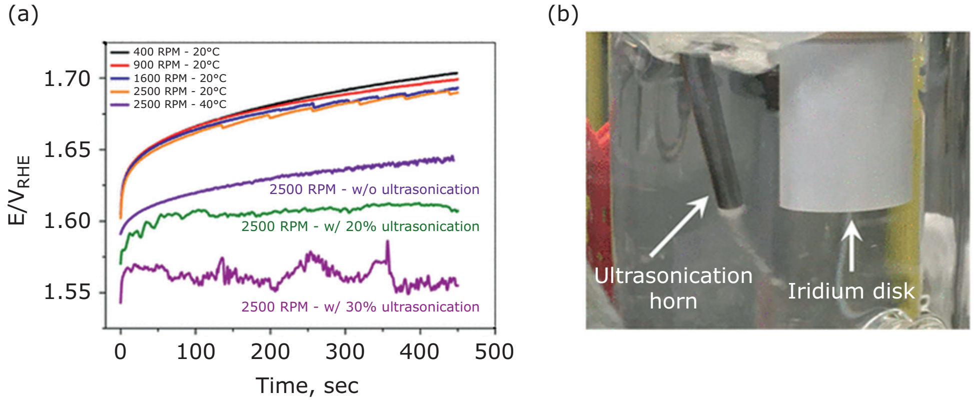

Fig. 7. (a) Effect of constant ultrasonication using setup; (b) on an iridium disc electrode. Only a limited increase in working electrode potential is observed as micro and macro bubbles of oxygen are removed by the effect of ultrasonication. Reproduced (Adapted) from Hartig-Weiss *et al.* (24). Copyright 2023 American Chemical Society

Figure 7(a) and **7(b)** to displace bubbles, showing that under constant potential the current density remained at its initial high value compared to the decrease that is seen under normal operation (24). Hartig-Weiss *et al.* (24) observed the same phenomenon during potential cycling studies (25). Ultimately, an ultrasonic probe is not a practical solution for aqueous model testing, as the mechanical force arising from cavitation can be sufficient to dislodge the catalyst adhered to the electrode substrate.

In addition, constant current operation is not the most severe mode of operation for many investigated catalysts, with start-up typically leading to a greater amount of dissolution (32, 103), although this increased dissolution may not be universal for all IrO_x based catalysts.

Work by Trogisch *et al.*, showed that catalyst dissolution was independent of catalyst loading across a range of different loading samples of the same catalyst (100–400 μg cm^{-2}) during CV-AST (200 cycles between 1.3–1.9 V$_{RHE}$) procedures but had a linear correlation when cycling outside of the OER region (0.05–1.4 V$_{RHE}$) (119). This was attributed to evolved gas shielding a comparable amount of the surface between different catalyst loading resulting in only a small thickness of the catalyst layer being exposed to dissolution conditions. Conversely, when cycling outside of the OER region all of the catalyst should be accessible and shows a linear dependence of iridium dissolution on catalyst loading. Although it should be noted that both oxygen saturated electrolyte was used alongside high loading, by aqueous model standards, as noted by authors which also contribute to increased proportion of catalyst being shielded from dissolution conditions.

2.1.3 Regeneration of Activity

Another electrochemical artefact that has been observed is the regeneration of activity after cycling or operation in the oxygen evolution region >1.4 V$_{RHE}$ without dropping below 1 V$_{RHE}$ and then cycling in region below 1 V$_{RHE}$ (122, 123) or leaving the catalyst for 30 min in flowing argon under open circuit voltage (OCV) (85, 124). Petzoldt *et al.* investigated this feature utilising the modified RDE technique to distinguish between reversible and irreversible catalyst degradation (85). Zheng *et al.* demonstrated this on $IrTaO_x$ where the catalyst on a gold substrate was held at 1.5 V$_{RHE}$ for five minutes resulting in a dramatic activity reduction followed by full regeneration after cycling to 0.9 V$_{RHE}$ (125).

There are several possible explanations for this observed regeneration. The first is that it is simply another effect of gas blinding and that cycling to lower potential reduces the oxygen concentration in these regions, allowing re-wetting of blocked catalyst surfaces. The modified RDE technique should overcome many of the issues relating to this type of surface blockage performance degradation, allowing for the high current density it observes (85). However, it is also possible that gas blinding is still an artifact that can occur in full cell testing of CCMs. Another explanation focuses around the effect of further oxidation of either the substrate gold (125) or catalyst. Zheng *et al.* attribute this to oxidation of the gold substrate on which the catalyst is supported. Another possible explanation is a reversible transformation in the catalyst itself (121, 124), such as conversion to an inactive or less active phase or segregation of the active component from the surface into the bulk.

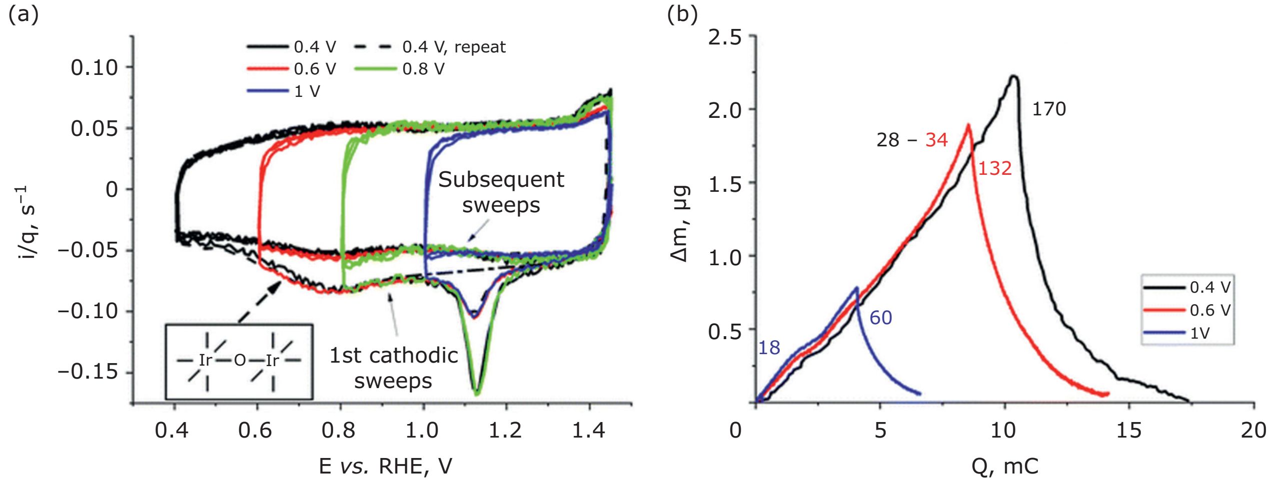

Fig. 8. Unsupported IrO_x Alfa Aesar catalyst showing: (a) cycles to various lower potential limits after period of OER; (b) mass changes accompanying cycles to various lower potential limits. Figure reproduced from Papakonstantinou *et al.* (123), under CC-BY 3.0 license

Papakonstantinou *et al.* (123), monitored mass changes that correspond with the cathodic cycle after a period of OER, see **Figure 8**. This change in mass during the cathodic cycle is cited as physical evidence, alongside the electrochemical regeneration of activity, for the reformatting (amorphisation) of the catalyst. Specifically, this is thought to be due to catalyst layer rehydration and reprotonation during reduction as the layer is dehydrated and deprotonated during operation at OER. This reformatting accompanies an increase in instability expected from more amorphous catalysts as noted by the authors.

The overall effect of this artifact, as highlighted by Petzoldt *et al.*, is that stability tests that cycle across the higher and lower potential regions (below 0.8–1 V) are more favourable for catalyst comparisons due to generating a greater amount of irreversible degradation (85). However, during operation in a real electrolyser system, dropping below 1 V_{RHE}, while possible during start-up and shutdown, would happen rarely. Ultimately, the regenerative effect is still not well understood and further studies are required to identify the exact reason behind it and to what extent it translates into full cell testing.

2.2 Stability Studies of CCMs

Electrochemical studies of MEA systems usually utilise a combination of CV (126), impedance spectroscopy (127) and polarisation curves (128) for activity measurement and longer periods of constant current or cycling for AST measurements. The most common studies of MEA level systems are often constant current operation over a period of 100–4000 h. While this may seem a relatively long time period, it still only represents a small fraction of the expected operational lifetime (>60,000+ h) (7). Just like AMS, AST is used to probe stability at the MEA level as it is not practical to test at this time frame on a large scale, outside of monitoring of commercial units. Instead, accelerated testing is conducted either utilising load cycling or reduced catalyst loading (or a combination) in order to simulate increased stress on either a single cell or stack (multiple MEA cells in one unit). One of the key limitations of full cell studies is knowing whether the changes observed are a result of anode catalyst degradation or other cell features, such as increasing contact resistance. While looking at general cell performance losses can provide valuable insight into the performance of different layers, decoupling some of the effects is essential.

2.2.1 Intermittent Operation of CCMs

Just like in aqueous model testing, intermittent operation is often used to accelerate the degradation of catalysts in full cell studies. Effects of intermittent operation have been investigated through cycling a MEA cell at different current densities and then allowing it to rest at OCV. In a study by Weiß *et al.*, conducted for 700 cycles between 3 A cm^{-2}, 0.1 A cm^{-2} and OCV, the initial 10 cycles showed an increase in performance attributed to the formation of surface layer of amorphous IrO_x due to H_2 crossover reducing the surface IrO_2 to iridium metal during the OCV stage and subsequent oxidising cycles forming the less stable but more active amorphous IrO_x (32). Over the course of the 700 cycles the performance decreased due to increasing high frequency resistance. This was attributed to both passivation of the titanium PTL, as observed in other studies, as well as decreased conductivity of the amorphous hydrous IrO_x versus the crystalline IrO_2 (76). When the OCV was replaced with a 1.3 V hold negligible degradation was observed over the course of 500 cycles, indicating that the change to OCV was responsible for degradation and that in operational systems this should try to mitigate against going to OCV where possible. Rakousky *et al.* (41) also reported increasing cell resistance over operation (approximately a 194 μVh^{-1} average degradation across 1000 h of operation with a titanium PTL). In follow up experiments where a platinum-coated titanium PTL was used instead the degradation was reduced significantly to 12 μVh^{-1}. Utilisation of a platinum-coated titanium PTL is common practice to prevent increasing contact resistance, allowing for a greater focus on degradation at the anode catalyst layer. Significant dissolution or crossover of the platinum in the platinum-coated PTL was not observed in studies utilising X-ray energy dispersive spectroscopy (XEDS) (38). Work by Anastasiia *et al.* investigated the effect of changing the lower voltage limit during AST testing on CCM with the cycling conducted between 2.2 V and various lower limits (120). Only cycling to 1.4 V cell voltage resulted in performance decay of 1 mV h^{-1} at 1 A cm^{-2} with 1.5 V resulting in an improving performance of –0.22 mV h^{-1} at 1 A cm^{-2}. This was ascribed to the lower potential limit resulting in degradation of cathode catalyst due to current reversal, a factor that typically does not occur in three electrode systems.

2.2.2 Effect of Iridium Oxidation State on Performance and Durability

The effect of iridium oxidation state, particularly during exposure to repeated reducing and oxidising conditions, can introduce additional factors that increase catalyst dissolution during intermittent operation versus dissolution from constant operation. Both in intermittent operation and in studies of different IrO_x based catalysts (129), the oxidation state is shown to have a significant effect on both the initial performance and how it changes over the first 1000 h of operation. Siracusano *et al.* studied Ir^0 (iridium black) and IrO_2 (0.34 mg_{Ir} cm^{-2} @ 1 A cm^{-2}) for a 1000 h endurance test, observing the Ir^0 having a significantly higher initial potential, 1.85–1.9 V, *vs.* 1.65 V of the IrO_2 catalyst. In addition to the initial performance difference the change during operation is different, with the iridium black seeing a higher initial change of performance of –72 μV h^{-1} before the rate stabilises at –26 μV h^{-1} and the IrO_2 seeing an initial rate of change in performance of 24 μV h^{-1} before stabilising at 12 μV h^{-1}. The better performance of the IrO_2 *vs.* iridium metal, is the reverse of the trend often observed in aqueous model testing (16, 35). The reverse is attributed to the higher oxidation state and the formation of a hydroxylated surface during operation that has higher performance, noted as an effect that has been observed repeatedly in the literature (16, 130, 131). Conversely, the iridium black undergoes improvement of activity over time likely due to oxidation of the surface iridium to the more active (59) hydrous oxide layer with higher oxidation state Ir^{3+}/Ir^{4+} observed in X-ray photoelectron spectroscopy (XPS) both before and after electrochemical testing.

2.2.3 Loading and Layer Effects

Currently, the loading of commercial PEMWE MEAs is around ~2 mg_{Ir} cm^{-2}, the required amount to maintain performance over lifetime (7, 34). Constant current studies by Rozain *et al.* looked at a series of IrO_2 MEAs that only differ by anode IrO_2 loading, ranging from 0.1–2.6 mg cm^{-2}. The MEA prepared with an anode loading at or above 0.5 mg cm^{-2} showed no dependence of cell voltage on loading during constant current measurements (132). Below 0.5 mg cm^{-2} increasing contact resistance is observed, likely due to problems with layer homogeneity and continuity. This difference has a greater relevance for both accelerated testing, when often lower loadings (≤0.3 mg_{Ir} cm^{-2}) are used to enhance degradation to make it easier to observe and quantify over shorter time periods, and for PEMWE technology as it is generally estimated that a reduction in catalyst loading of over an order of magnitude is required to achieve long term commercial viability of the technology. In order to mitigate against this low loading effect it was shown that for low anode loadings (<0.5 mg cm^{-2}) the addition of micro-sized titanium particles (IrO_2/Ti 50 wt% IrO_2) could improve the performance and stability of cells (78). This was attributed to the titanium particles improving electron transfer between the current collector and the catalyst and resulted in both a smaller Ohmic resistance of 230 mΩ cm^2 @ 0.12 mg cm^{-2} for IrO_2/Ti, *vs.*

350 mΩ cm^2 @ 0.1 mg cm^{-2} for pure IrO_2. The ohmic resistance was also stabilised, not increasing significantly over 1500 h of operation. Solutions like this that maintain the conductivity of the layer will be increasingly important going to thinner (lower loading) layers (37).

2.3 Complementary Techniques

Due to experimental artifacts, electrochemical tests on their own are insufficient when investigating stability of PEMWE catalysts, especially in regions where dissolution can occur. As mentioned, IrO_x represents some of the most stable catalysts, and this represents a challenge when trying to quantify catalyst losses due to the small quantities being dissolved often resulting in only parts per billion changes to the iridium content of the electrolyte solutions (92, 112).

Two common complementary techniques used for investigating OER catalyst mass loss were investigated by Frydendal *et al.* (92): the electrochemical quartz crystal microbalance (EQCM) (93) and ICP-MS. Together they can be used to distinguish the two primary sources of mass loss, detachment and dissolution (92). EQCM monitors all mass changes at the electrode, which covers both iridium lost through nanoparticle detachment and that from dissolution and oxide growth/losses. ICP-MS on the other hand can only detect dissolved iridium ions, meaning that any metallic iridium arising from nanoparticle detachment is not detected. For other metals, a common technique in ICP-MS is to use strong acid to dissolve any solid metal entrained in the solution, such as detached nanoparticles. However, iridium has exceptional stability in acidic environments, with some forms not even undergoing dissolution in *aqua regia* (133). It is also worth pointing out that some more modern ICP-MS instruments have the capability of detecting and analysing nanoparticle size; this is typically only for particles greater than 10 nm (134).

Detachment may be of less importance to the investigation of catalyst stability than dissolution (92), as while electro-flaking can occur in MEAs, the process is likely to be very different to that of RDE studies in which the catalyst is adhered to a solid planar surface using a PFSA layer. ICP-MS is often used as the primary technique for the investigation of catalyst dissolution (25, 86, 88, 92). Coupled with the low detection limit in the parts per billion region (92), with more modern machines being able to detect iridium to the parts per trillion level, this makes it one of the few techniques suitable for quantitative analysis of dissolved catalyst material.

Investigation of catalyst stability can be taken further with the use of *operando* ICP-MS (13, 27, 112). Work by Geiger *et al.* combined the use of a SFC and ICP-MS to investigate the catalyst degradation mechanism and benchmark stability of OER catalysts using near real time measurements of iridium dissolution (28). By utilising high sensitivity techniques such as online ICP-MS coupled with a SFC, it is possible to look at OER catalyst dissolution over relatively short periods of time, typically ranging from several minutes to several hours (112). Over short time periods these investigations have demonstrated that for many types of iridium-based catalysts there is a large amount of dissolution during the initial application of current/potential in the OER region, before dropping to a lower level of dissolution at higher potentials. This is particularly relevant for metallic iridium (87) and hydrothermally prepared iridium oxide (88), which both exhibit this initial increased dissolution rate at lower overpotentials. These results have been confirmed by taking electrolyte samples from a stagnant EC-MS cell as well, indicating that they are not an artifact of the electrolyte flow (58). The instability of hydrothermally prepared iridium oxides and metallic iridium is often explained by the presence of a greater proportion of lower oxidation state iridium (Ir, Ir^{III}), since thermally prepared anhydrous IrO_x, which have a much lower presence of lower oxidation state species (predominantly Ir^{IV} in the form IrO_2) are much more stable but do not exhibit as high activity (13, 59). Although it is also argued that other factors also effect stability such as: (i) distortion in the IrO_6 geometry (54); (ii) lattice strain (135); and (iii) the presence of short-range order interconnected hollandite clusters (136). One of the general conclusions both from these results (28) but also from other stability testing (29) is that, while it is possible to measure catalyst dissolution rates very accurately, this is only suitable for identifying trends between catalysts and is not capable of determining the lifetime in a real system, often underestimating lifetime by orders of magnitude (22).

Further studies utilising online SFC ICP-MS have investigated the effect of a range of parameters on the S-number using a baseline 10 μg cm^{-2} loading of IrO_x (**Figure 9**). Little effect of loading (10–250 μg cm^{-2}) or flow rate (66–740 μl min^{-1}) on the S-number was observed. The effect of Nafion® content on iridium content in solution was

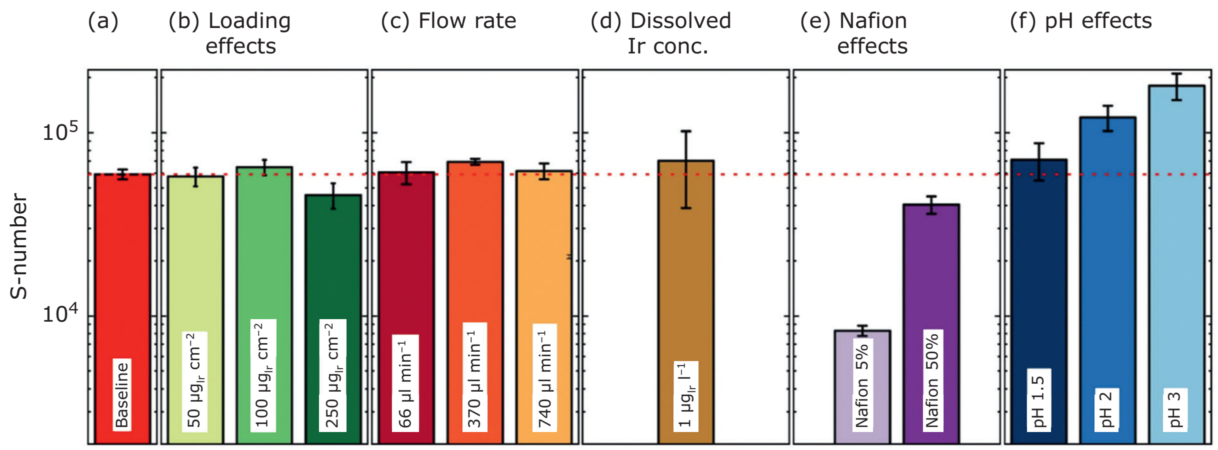

Fig. 9. The effect on S-Number (O_2 evolved (from current) / dissolved iridium (from online ICP-MS)) of varying parameters utilising deposited catalyst layer in SFC connected to online ICP-MS: (a) baseline; (b) varying catalyst loading; (c) electrolyte flow rate; (d) electrolyte saturated with dissovled iridium; (e) varying Nafion® content; (f) varying pH of electrolyte. Reproduced from Knöppel *et al.* (22), under CC-BY 4.0 international license

hypothesised to be a result of reduced mobility of dissolved iridium in Nafion®; at higher content the greater localised iridium content makes dissolution less favourable. This hypothesis requires further experimental evidence regarding the effect of larger localised iridium content impeding dissolved iridium movement versus the increased volume of Nafion® acting as an iridium sink, thus preventing a greater amount of iridium from being detected. This phenomenon is especially important to take into account when considering that increasing the Ir^{x+} content of the electrolyte artificially, by the inclusion of dissolved iridium, had no noticeable effect on the recorded dissolution rate (**Figure 9(d)**).

The rotating ring disc electrode (RRDE) is another model system technique that has been used to explore performance and stability of OER catalysts (82, 83, 105). This differs from conventional RDE by effectively having a second working electrode which can, *via* a secondary reaction, be used to probe the products formed from the main catalyst layer, albeit proportionally with a given collection efficiency. This has been applied to ruthenium-based catalysts using two different approaches; firstly, for the determination of faradaic efficiency toward oxygen generation *via* reduction of evolved oxygen at a platinum ring held at standard oxygen reduction conditions ~0.6 V_{RHE}. The second approach involves the collection of dissolved species at the ring by holding the potential (@0.9 V_{RHE} for dissolved Ru^{4+}) (105) and monitoring the current obtained, which corresponds to the deposition of the metal. The work by Danilovic *et al.* did compare the faradaic efficiency difference between polycrystalline ruthenium and iridium, finding a 10% and 1% efficiency toward dissolution of the different elements, respectively (105). As ruthenium-based catalysts are often orders of magnitude less stable (15) than IrO_x it is unlikely that this technique could be used for the detection of dissolved iridium, especially for the more stable thermally prepared oxides. However, validation of the ability of the RRDE to determine faradaic efficiency with EC-MS (95) could be useful in confirming whether it can distinguish evolved oxygen. Alternatively, EC-MS (125) could be used on its own for screening candidate catalyst materials to ensure high faradaic efficiency (>99%) toward the OER of novel electrocatalysts that might have high current contributions from other processes (137, 138).

Ex situ characterisation techniques can also complement AST, for example identical location transmission electron microscopy (IL-TEM) and XPS coupled with AST up to 50,000 cycles between 1.2 V_{RHE} and 1.6 V_{RHE}. The studies conducted by Claudel *et al.* (96) of potential cycling on IrO_x based catalysts supported on Vulcan® XC72 carbon and antimony-doped tin oxide (ATO) highlighted that dissolution of nanoparticles was particularly likely in the conditioning phase of the test, which consisted of 100 cycles between 0.05 V_{RHE} and 1.4 V_{RHE}, with this dissolution likely due to the increased instability of lower oxidation state iridium (0, 3+) undergoing reduction and oxidation. From the longer period of cycling it was inferred that instability of the support led to the majority of catalyst losses, especially for the carbon-supported catalysts due to oxidation of carbon. Alongside carbon supports, which are predictably unstable, metal oxide-based supports were also demonstrated to be unstable over cycling, showing that for stability studies of supported nanoparticles, even on state-of-the-art OER supports (139), the support itself might function as the limiting factor of the stability of the catalyst (96) due to instability of the support typically from leaching of the dopant (106, 140). Ensuring that the support demonstrates comparable or greater stability to dissolution as the catalyst will be key in utilising the increased performance available from the greater catalyst dispersion that supports provide.

2.4 Post-Mortem Characterisation

In MEA testing, measuring dissolved iridium in feed out water to quantify catalyst dissolution rates is challenging due to the varying nature of the water systems, recirculation, water crossover (from anode to cathode side) and the preference for dissolved iridium to also migrate into the membrane (38) or redeposit on any metal in the water recirculation loop (22). Post-mortem characterisation of the MEA is carried out to assess the degradation of the anode and cathode catalysts from long term and accelerated degradation testing. Often variants of *ex situ* analysis include scanning electron microscopy (SEM) combined with energy dispersive X-ray (EDX) spectroscopy, and/or electron energy loss spectroscopy (EELS) in order to look at the elemental composition across the MEA to determine the extent of catalyst dissolution across the membrane as well as degradation of the membrane itself (41), which can result in increased gas crossover. Techniques such as X-ray scattering can also be used to investigate catalyst structure changes (43).

A study by Yu *et al.* monitored iridium and platinum dissolution into the membrane after 4000 h of operation of a CCM with low anode catalyst loading of 0.3 mg_{Ir} cm^{-2}, utilising SEM, STEM and EDX to determine distribution of the catalyst across the MEA (38). **Figure 10** shows the distribution across the MEA with 30% remaining at the anode while another 10% redeposits in an IrO_x band at the anode membrane interface that still maintains its catalytic activity; however, 18% was found to cross and redeposit in the membrane and a further 42% was found to cross the membrane and deposit on the cathode side as metallic iridium. Iridium-platinum particles form in the membrane due to hydrogen reducing the dissolved metal ions causing them to plate out during periods of interruption. While these results are likely an exaggeration of current stability performance because of low loading, they do illustrate the driving force for the dissolved iridium to cross the membrane (travelling to the cathode) in an operational system. They could also illustrate a failure mechanism as metal redepositing in the membrane will increase the ohmic resistance, reduce the mechanical integrity in the membrane, and potentially increase gas crossover (141).

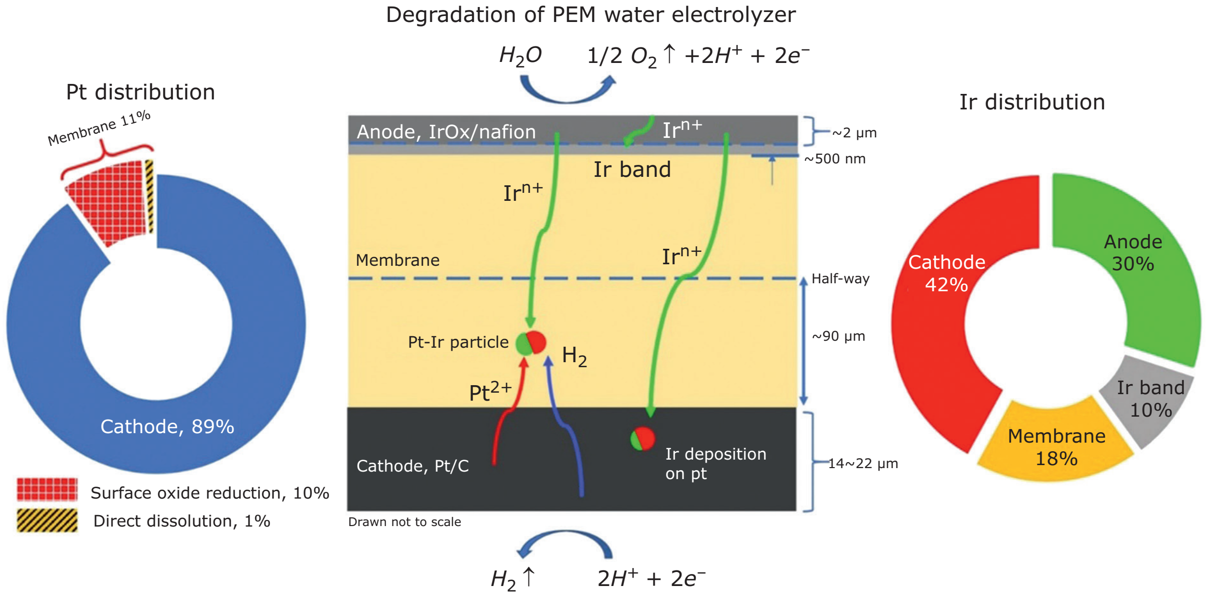

Fig. 10. Distribution of iridium and platinum in a degraded CCM. The proportion of iridium in each location was determined by SEM-XEDS. Reprinted from Yu *et al.* (38) Copyright (2023), with permission from Elsevier

Just as *ex situ* TEM can be used for AMS (96, 142) it can also be conducted post-mortem on CCM (143). This allows for a more detailed look at how the catalyst or membrane is being affected, with the ability to investigate individual nanoparticles while sacrificing the scale of SEM. Typically these would be used in conjunction, with SEM providing resolution across the entire CCM and at interfacial regions and TEM being used at specific points to investigate catalyst particle change.

Part II (144) will highlight considerations and best practices for the investigation of activity and stability of oxygen evolution catalysts *via* short term testing.

Acknowledgement

We would like to acknowledge the Engineering and Physical Sciences Council for an industrial CASE studentship with contributions from National Physical Laboratory and Johnson Matthey. This work was partly supported by the National Measurement System of the UK Department of Business, Energy & Industrial Strategy. SBS was also supported in part by by the Marie Sklodowska Curie Actions and Iberdrola Group, Grant Agreement №101034297.

References

1. 'Hydrogen for Net-Zero: A Critical Cost-Competitive Energy Vector', Hydrogen Council, Brussels, Belgium, McKinsey & Company, New York, USA, November, 2021, 56 pp
2. "Green Hydrogen: A Guide to Policy Making", IRENA (International Renewable Energy Agency), Abu Dhabi, United Arab Emiriates, 2020, 52 pp
3. "Hydrogen-Powered Aviation: A Fact-Based Study of Hydrogen Technology, Economics, and Climate Impact by 2050", Clean Sky 2 JU, Brussels, Belguim, Fuel Cells and Hydrogen Join Undertaking (CBH 2 JU), Brussels, Belguim, 2020, 96 pp
4. G. Pawelec, J. Fonseca, "Steel From Solar Energy: A Techno-Economic Assessment of Green Steel Manufacturing", Hydrogen Europe, Brussels, Belgium, 2022, 90 pp
5. K. Mazloomi, C. Gomes, *Renew. Sustain. Energy Rev.*, 2012, **16**, (5), 3024
6. 'HyDeploy Project: Gas Network Innovation Competition: Cadent Second Project Progress Report (PPR)', HyDeploy, Keele University, Keele, UK, December, 2018, 28 pp
7. L. Bertuccioli, A. Chan, D. Hart, F. Lehner, B. Madden, E. Standen, "Development of Water Electrolysis in the European Union", Fuel Cells and Hydrogen Joint Undertaking, Institution of Gas Engineers and Managers, Brussels, Belgium, 2014
8. M. Voldsund, K. Jordal, R. Anantharaman, *Int. J. Hydrogen Energy*, 2016, **41**, (9), 4969
9. P. C. K. Vesborg, T. F. Jaramillo, *RSC Adv.*, 2012, **2**, (21), 7933
10. K. Ayers, N. Danilovic, R. Ouimet, M. Carmo, B. Pivovar, M. Bornstein, *Annu. Rev. Chem. Biomol. Eng.*, 2019, **10**, 219
11. U. Babic, M. Suermann, F. N. Büchi, L. Gubler, T. J. Schmidt, *J. Electrochem. Soc.*, 2017, **164**, (4), F387
12. K. Ayers, *Curr. Opin. Chem. Eng.*, 2021, **33**, 100719
13. S. Geiger, O. Kasian, B. R. Shrestha, A. M. Mingers, K. J. J. Mayrhofer, S. Cherevko, *J. Electrochem. Soc.*, 2016, **163**, (11), F3132
14. K. E. Ayers, L. T. Dalton, E. B. Anderson, *ECS Trans.*, 2012, **41**, (33), 27
15. S. Cherevko, A. R. Zeradjanin, A. A. Topalov, N. Kulyk, I. Katsounaros, K. J. J. Mayrhofer, *ChemCatChem*, 2014, **6**, (8), 2219
16. S. Cherevko, S. Geiger, O. Kasian, N. Kulyk, J.-P. Grote, A. Savan, B. R. Shrestha, S. Merzlikin, B. Breitbach, A. Ludwig, K. J. J. Mayrhofer, *Catal. Today*, 2016, **262**, 170
17. L. Bloxham, S. Brown, L. Cole, A. Cowley, M. Fujita, N. Girardot, J. Jiang, M. Ryan, B. Tang, A. Wang, "PGM Market Report", Johnson Matthey Plc, London, UK, May, 2022, 60 pp
18. M. Clapp, C. M. Zalitis, M. Ryan, *Catal. Today*, 2023, **420**, 114140
19. M. Bernt, A. Siebel, H. A. Gasteiger, *J. Electrochem. Soc.*, 2018, **165**, (5), F305
20. A. Nilsson, I. Stephens, 'Sustainable N_2 Reduction', in "Research Needs Towards Sustainable Production of Fuels and Chemicals", eds. A. Latimer, C. F. Dickens, Section 5, Energy-X, San Juan, Puerto Rico, 2019, pp. 49–59
21. S. M. Alia, S. Stariha, R. L. Borup, *J. Electrochem. Soc.*, 2019, **166**, (15), F1164
22. J. Knöppel, M. Möckl, D. Escalera-López, K. Stojanovski, M. Bierling, T. Böhm, S. Thiele, M. Rzepka, S. Cherevko, *Nat. Commun.*, 2021, **12**, 2231
23. T. Lazaridis, B. M. Stühmeier, H. A. Gasteiger, H. A. El-Sayed, *Nat. Catal.*, 2022, **5**, (5), 363
24. A. Hartig-Weiss, M. F. Tovini, H. A. Gasteiger, H. A. El-Sayed, *ACS Appl. Energy Mater.*, 2020, **3**, (11), 10323
25. H. A. El-Sayed, A. Weiß, L. F. Olbrich, G. P. Putro, H. A. Gasteiger, *J. Electrochem. Soc.*, 2019, **166**, (8), F458

26. K. Ehelebe, D. Escalera-López, S. Cherevko, *Curr. Opin. Electrochem.*, 2021, **29**, 100832
27. J.-P. Grote, A. R. Zeradjanin, S. Cherevko, K. J. J. Mayrhofer, *Rev. Sci. Instrum.*, 2014, **85**, (10), 104101
28. S. Geiger, O. Kasian, M. Ledendecker, E. Pizzutilo, A. M. Mingers, W. T. Fu, O. Diaz-Morales, Z. Li, T. Oellers, L. Fruchter, A. Ludwig, K. J. J. Mayrhofer, M. T. M. Koper, S. Cherevko, *Nat. Catal.*, 2018, **1**, (7), 508
29. M. F. Tovini, A. Hartig-Weiß, H. A. Gasteiger, H. A. El-Sayed, *J. Electrochem. Soc.*, 2021, **168**, (1), 014512
30. A. K. S. Kumar, Y. Zhang, D. Li, R. G. Compton, *Electrochem. Commun.*, 2020, **121**, 106867
31. B. Pivovar, M. Ruth, R. Ahluwalia, 'H2NEW: Hydrogen (H2) from Next-generation Electrolyzers of Water LTE Task 3c : System and Techno-Economic Analysis', DOE Hydrogen Program Project ID No. P196D, Annual Merit Review and Peer Evaluation Meeting, 6th–8th June, 2022, National Renewable Energy Laboratory, Golden, USA, 2nd June, 2022
32. A. Weiß, A. Siebel, M. Bernt, T.-H. Shen, V. Tileli, H. A. Gasteiger, *J. Electrochem. Soc.*, 2019, **166**, (8), F487
33. E. Brightman, J. Dodwell, N. van Dijk, G. Hinds, *Electrochem. Commun.*, 2015, **52**, 1
34. M. Bernt, H. A. Gasteiger, *J. Electrochem. Soc.*, 2016, **163**, (11), F3179
35. S. M. Alia, G. C. Anderson, *J. Electrochem. Soc.*, 2019, **166**, (4), F282
36. S. M. Alia, M.-A. Ha, G. C. Anderson, C. Ngo, S. Pylypenko, R. E. Larsen, *J. Electrochem. Soc.*, 2019, **166**, (15), F1243
37. M. Möckl, M. F. Ernst, M. Kornherr, F. Allebrod, M. Bernt, J. Byrknes, C. Eickes, C. Gebauer, A. Moskovtseva, H. A. Gasteiger, *J. Electrochem. Soc.*, 2022, **169**, (6), 064505
38. H. Yu, L. Bonville, J. Jankovic, R. Maric, *Appl. Catal. B: Environ.*, 2020, **260**, 118194
39. G. N. Martelli, R. Ornelas, G. Faita, *Electrochim. Acta*, 1994, **39**, (11–12), 1551
40. C. Liu, 'Noble Metal Coated Porous Transport Layers for Polymer Electrolyte Membrane Water Electrolysis', PhD Thesis, Faculty of Mechanical Engineering, Rhenish-Westphalian Technical University, Aachen, Germany, 2021, 149 pp
41. C. Rakousky, U. Reimer, K. Wippermann, M. Carmo, W. Lueke, D. Stolten, *J. Power Sources*, 2016, **326**, 120
42. J. Durst, C. Simon, F. Hasché, H. A. Gasteiger, *J. Electrochem. Soc.*, 2014, **162**, (1), F190
43. S. M. Alia, K. S. Reeves, H. Yu, J. Park, N. Kariuki, A. J. Kropf, D. J. Myers, D. A. Cullen, *J. Electrochem. Soc.*, 2022, **169**, (5), 054517
44. T. Reier, H. N. Nong, D. Teschner, R. Schlögl, P. Strasser, *Adv. Energy Mater.*, 2016, **7**, (1), 1601275
45. C. Spöri, J. T. H. Kwan, A. Bonakdarpour, D. P. Wilkinson, P. Strasser, *Angew. Chem. Int. Ed.*, 2017, **56**, (22), 5994
46. O. Kasian, J.-P. Grote, S. Geiger, S. Cherevko, K. J. J. Mayrhofer, *Angew. Chem. Int. Ed.*, 2018, **57**, (9), 2488
47. C. Bozal-Ginesta, R. R. Rao, C. A. Mesa, Y. Wang, Y. Zhao, G. Hu, D. Antón-García, I. E. L. Stephens, E. Reisner, G. W. Brudvig, D. Wang, J. R. Durrant, *J. Am. Chem. Soc.*, 2022, **144**, (19), 8454
48. S. W. Sheehan, J. M. Thomsen, U. Hintermair, R. H. Crabtree, G. W. Brudvig, C. A. Schmuttenmaer, *Nat. Commun.*, 2015, **6**, 6469
49. M. Ledendecker, S. Geiger, K. Hengge, J. Lim, S. Cherevko, A. M. Mingers, D. Göhl, G. V Fortunato, D. Jalalpoor, F. Schüth, C. Scheu, K. J. J. Mayrhofer, *Nano Res.*, 2019, **12**, (9), 2275
50. L. C. Seitz, C. F. Dickens, K. Nishio, Y. Hikita, J. Montoya, A. Doyle, C. Kirk, A. Vojvodic, H. Y. Hwang, J. K. Norskov, T. F. Jaramillo, *Science*, 2016, **353**, (6303), 1011
51. A. Grimaud, A. Demortière, M. Saubanère, W. Dachraoui, M. Duchamp, M.-L. Doublet, J.-M. Tarascon, *Nat. Energy*, 2017, **2**, (1), 16189
52. W. Sun, Y. Song, X.-Q. Gong, L. Cao, J. Yang, *ACS Appl. Mater. Interfaces*, 2016, **8**, (1), 820
53. K. Sardar, E. Petrucco, C. I. Hiley, J. D. B. Sharman, P. P. Wells, A. E. Russell, R. J. Kashtiban, J. Sloan, R. I. Walton, *Angew. Chem. Int. Ed.*, 2014, **53**, (41), 10960
54. W. Sun, J.-Y. Liu, X.-Q. Gong, W.-Q. Zaman, L.-M. Cao, J. Yang, *Sci. Rep.*, 2016, **6**, 38429
55. D. Lebedev, M. Povia, K. Waltar, P. M. Abdala, I. E. Castelli, E. Fabbri, M. V. Blanco, A. Fedorov, C. Copéret, N. Marzari, T. J. Schmidt, *Chem. Mater.*, 2017, **29**, (12), 5182
56. H. Liu, Z. Zhang, M. Li, Z. Wang, X. Zhang, T. Li, Y. Li, S. Tian, Y. Kuang, X. Sun, *Small*, 2022, **18**, (30), 2202513
57. F. G. Sen, A. Kinaci, B. Narayanan, S. K. Gray, M. J. Davis, S. K. R. S. Sankaranarayanan, M. K. Y. Chan, *J. Mater. Chem. A*, 2015, **3**, (37), 18970
58. S. B. Scott, J. E. Sørensen, R. R. Rao, C. Moon, J. Kibsgaard, Y. Shao-Horn, I. Chorkendorff, *Energy Environ. Sci.*, 2022, **15**, (5), 1988
59. D. F. Abbott, D. Lebedev, K. Waltar, M. Povia, M. Nachtegaal, E. Fabbri, C. Copéret, T. J. Schmidt,

Chem. Mater., 2016, **28**, (18), 6591

60. G. C. da Silva, N. Perini, E. A. Ticianelli, *Appl. Catal. B: Environ.*, 2017, **218**, 287
61. S. Fierro, T. Nagel, H. Baltruschat, C. Comninellis, *Electrochem. Commun.*, 2007, **9**, (8), 1969
62. O. Kasian, S. Geiger, T. Li, J.-P. Grote, K. Schweinar, S. Zhang, C. Scheu, D. Raabe, S. Cherevko, B. Gault, K. J. J. Mayrhofer, *Energy Environ. Sci.*, 2019, **12**, (12), 3548
63. S. B. Scott, J. Kibsgaard, P. C. K. Vesborg, I. Chorkendorff, *Electrochim. Acta*, 2021, **374**, 137844
64. C. Felix, B. Bladergroen, V. Linkov, B. G. Pollet, S. Pasupathi, *Catalysts*, 2019, **9**, (4), 318
65. T. Binninger, R. Mohamed, K. Waltar, E. Fabbri, P. Levecque, R. Kötz, T. J. Schmidt, *Sci. Rep.*, 2015, **5**, 12167
66. C. Roy, R. R. Rao, K. A. Stoerzinger, J. Hwang, J. Rossmeisl, I. Chorkendorff, Y. Shao-Horn, I. E. L. Stephens, *ACS Energy Lett.*, 2018, **3**, (9), 2045
67. E. Özer, C. Spöri, T. Reier, P. Strasser, *ChemCatChem*, 2017, **9**, (4), 597
68. M. Scohy, S. Abbou, V. Martin, B. Gilles, E. Sibert, L. Dubau, F. Maillard, *ACS Catal.*, 2019, **9**, (11), 9859
69. A. BalaKrishnan, N. Blanc, U. Hagemann, P. Gemagami, K. Wonner, K. Tschulik, T. Li, *Angew. Chem.*, 2021, **133**, (39), 21566
70. A. Lončar, D. Escalera-López, S. Cherevko, N. Hodnik, *Angew. Chem.*, 2022, **134**, (14), e202114437
71. M. J. N. Pourbaix, J. Van Muylde, N. de Zoubov, *Platinum Metals Rev*., 1959, **3**, (3), 100
72. Z. Wang, Y.-R. Zheng, I. Chorkendorff, J. K. Nørskov, *ACS Energy Lett.*, 2020, **5**, (9), 2905
73. S. Cherevko, *J. Electroanal. Chem.*, 2017, **787**, 11
74. A. S. Raman, A. Vojvodic, *J. Phys. Chem. C*, 2022, **126**, (2), 922
75. "Green Hydrogen Cost Reduction: Scaling Up Electrolysers to meet the 1.5ºC Climate Goal", IRENA (International Renewable Energy Agency), Abu Dhabi, Dubai, December, 2020
76. E. Rasten, G. Hagen, R. Tunold, *Electrochim. Acta*, 2003, **48**, (25–26), 3945
77. H. Yu, N. Danilovic, Y. Wang, W. Willis, A. Poozhikunnath, L. Bonville, C. Capuano, K. Ayers, R. Maric, *Appl. Catal. B: Environ.*, 2018, **239**, 133
78. C. Rozain, E. Mayousse, N. Guillet, P. Millet, *Appl. Catal. B: Environ.*, 2016, **182**, 123
79. S. Siracusano, N. Van Dijk, R. Backhouse, L. Merlo, V. Baglio, A. S. Aricò, *Renew. Energy*, 2018, **123**, 52
80. A. J. Bard, L. R. Faulkner, "Electrochemical Methods: Fundamentals and Applications", 2nd Edn., John Wiley and Sons Inc, New York, USA, 2001, 864 pp
81. T. Ioroi, T. Nagai, Z. Siroma, K. Yasuda, *Int. J. Hydrogen Energy*, 2022, **47**, (91), 38506
82. R. Kötz, S. Stucki, D. Scherson, D. M. Kolb, *J. Electroanal. Chem. Interfacial Electrochem.*, 1984, **172**, (1–2), 211
83. M. Vuković, *J. Chem. Soc., Faraday Trans.*, 1990, **86**, (22), 3743
84. M. Kroschel, A. Bonakdarpour, J. T. H. Kwan, P. Strasser, D. P. Wilkinson, *Electrochim. Acta*, 2019, **317**, 722
85. P. J. Petzoldt, J. T. H. Kwan, A. Bonakdarpour, D. P. Wilkinson, *J. Electrochem. Soc.*, 2021, **168**, (2), 026507
86. S. Cherevko, T. Reier, A. R. Zeradjanin, Z. Pawolek, P. Strasser, K. J. J. Mayrhofer, *Electrochem. Commun.*, 2014, **48**, 81
87. S. Cherevko, S. Geiger, O. Kasian, A. Mingers, K. J. J. Mayrhofer, *J. Electroanal. Chem.*, 2016, **773**, 69
88. S. Cherevko, S. Geiger, O. Kasian, A. Mingers, K. J. J. Mayrhofer, *J. Electroanal. Chem.*, 2016, **774**, 102
89. C. M. Zalitis, D. Kramer, A. R. Kucernak, *Phys. Chem. Chem. Phys.*, 2013, **15**, (12), 4329
90. M. Inaba, A. W. Jensen, G. W. Sievers, M. Escudero-Escribano, A. Zana, M. Arenz, *Energy Environ. Sci.*, 2018, **11**, (4), 988
91. A. Hrnjić, F. Ruiz-Zepeda, M. Gaberšček, M. Bele, L. Suhadolnik, N. Hodnik, P. Jovanovič, *J. Electrochem. Soc.*, 2020, **167**, (16), 166501
92. R. Frydendal, E. A. Paoli, B. P. Knudsen, B. Wickman, P. Malacrida, I. E. L. Stephens, I. Chorkendorff, *ChemElectroChem*, 2014, **1**, (12), 2075
93. D. A. Buttry, M. D. Ward, *Chem. Rev.*, 1992, **92**, (6), 1355
94. R. Frydendal, E. A. Paoli, I. Chorkendorff, J. Rossmeisl, I. E. L. Stephens, *Adv. Energy Mater.*, 2015, **5**, (22), 1500991
95. D. B. Trimarco, S. B. Scott, A. H. Thilsted, J. Y. Pan, T. Pedersen, O. Hansen, I. Chorkendorff, P. C. K. Vesborg, *Electrochim. Acta*, 2018, **268**, 520
96. F. Claudel, L. Dubau, G. Berthomé, L. Sola-

Hernandez, C. Beauger, L. Piccolo, F. Maillard, *ACS Catal.*, 2019, **9**, (5), 4688

97. C. C. L. McCrory, S. Jung, J. C. Peters, T. F. Jaramillo, *J. Am. Chem. Soc.*, 2013, **135**, (45), 16977
98. C. C. L. McCrory, S. Jung, I. M. Ferrer, S. M. Chatman, J. C. Peters, T. F. Jaramillo, *J. Am. Chem. Soc.*, 2015, **137**, (13), 4347
99. W. Gou, M. Zhang, Y. Zou, X. Zhou, Y. Qu, *ChemCatChem*, 2019, **11**, (24), 6008
100. L. Li, P. Wang, Z. Cheng, Q. Shao, X. Huang, *Nano Res.*, 2022, **15**, (2), 1087
101. Z. Wang, Z. Zheng, Y. Xue, F. He, Y. Li, *Adv. Energy Mater.*, 2021, **11**, (32), 2170126
102. Y. Chen, H. Li, J. Wang, Y. Du, S. Xi, Y. Sun, M. Sherburne, J. W. Ager, A. C. Fisher, Z. J. Xu, *Nat. Commun.*, 2019, **10**, 572
103. C. Spöri, C. Brand, M. Kroschel, P. Strasser, *J. Electrochem. Soc.*, 2021, **168**, (3), 034508
104. G. Tsotridis, A. Pilenga, "EU Harmonized Protocols for Testing of Low Temperature Water Electrolysis", JRC Technical Report No. JRC122565, European Commission, Petten, The Netherlands, 2021, 171 pp
105. N. Danilovic, R. Subbaraman, K.-C. Chang, S. H. Chang, Y. J. Kang, J. Snyder, A. P. Paulikas, D. Strmcnik, Y.-T. Kim, D. Myers, V. R. Stamenkovic, N. M. Markovic, *J. Phys. Chem. Lett.*, 2014, **5**, (14), 2474
106. C. D. Ferreira da Silva, F. Claudel, V. Martin, R. Chattot, S. Abbou, K. Kumar, I. Jiménez-Morales, S. Cavaliere, D. Jones, J. Rozière, L. Solà-Hernandez, C. Beauger, M. Faustini, J. Peron, B. Gilles, T. Encinas, L. Piccolo, F. H. Barros de Lima, L. Dubau, F. Maillard, *ACS Catal.*, 2021, **11**, (7), 4107
107. J. Edgington, A. Deberghes, L. C. Seitz, *ACS Appl. Energy Mater.*, 2022, **5**, (10), 12206
108. C. Wei, S. Sun, D. Mandler, X. Wang, S. Z. Qiao, Z. J. Xu, *Chem. Soc. Rev.*, 2019, **48**, (9), 2518
109. S. Watzele, P. Hauenstein, Y. Liang, S. Xue, J. Fichtner, B. Garlyyev, D. Scieszka, F. Claudel, F. Maillard, A. S. Bandarenka, *ACS Catal.*, 2019, **9**, (10), 9222
110. O. Kasian, T. Li, A. M. Mingers, K. Schweinar, A. Savan, A. Ludwig, K. Mayrhofer, *J. Phys. Energy*, 2021, **3**, (3), 034006
111. O. Kasian, S. Geiger, P. Stock, G. Polymeros, B. Breitbach, A. Savan, A. Ludwig, S. Cherevko, K. J. J. Mayrhofer, *J. Electrochem. Soc.*, 2016, **163**, (11), F3099
112. O. Kasian, S. Geiger, K. J. J. Mayrhofer, S. Cherevko, *Chem. Rec.*, 2019, **19**, (10), 2130
113. O. Kasian, S. Geiger, M. Schalenbach, A. M. Mingers, A. Savan, A. Ludwig, S. Cherevko, K. J. J. Mayrhofer, *Electrocatalysis*, 2018, **9**, (2), 139
114. R. Zhang, P. E. Pearce, V. Pimenta, J. Cabana, H. Li, D. A. D. Corte, A. M. Abakumov, G. Rousse, D. Giaume, M. Deschamps, A. Grimaud, *Chem. Mater.*, 2020, **32**, (8), 3499
115. R. Zhang, N. Dubouis, M. B. Osman, W. Yin, M. T. Sougrati, D. A. D. Corte, D. Giaume, A. Grimaud, *Angew. Chem. Int. Ed.*, 2019, **58**, (14), 4571
116. S. Geiger, O. Kasian, A. M. Mingers, S. S. Nicley, K. Haenen, K. J. J. Mayrhofer, S. Cherevko, *ChemSusChem*, 2017, **10**, (21), 4140
117. M. Bernt, A. Hartig-Weiß, M. F. Tovini, H. A. El-Sayed, C. Schramm, J. Schröter, C. Gebauer, H. A. Gasteiger, *Chem. Ing. Tech.*, 2020, **92**, (1–2), 31
118. E. Oakton, D. Lebedev, M. Povia, D. F. Abbott, E. Fabbri, A. Fedorov, M. Nachtegaal, C. Copéret, T. J. Schmidt, *ACS Catal.*, 2017, **7**, (4), 2346
119. N. Trogisch, M. Koch, E. N. El Sawy, H. A. El-Sayed, *ACS Catal.*, 2022, **12**, (21), 13715
120. A. Voronova, H.-J. Kim, J. H. Jang, H.-Y. Park, B. Seo, *Int. J. Energy Res.*, 2022, **46**, (9), 11867
121. G. Papakonstantinou, G. Algara-Siller, D. Teschner, T. Vidaković-Koch, R. Schlögl, K. Sundmacher, *Appl. Energy*, 2020, **280**, 115911
122. R. Tang-Kong, C. E. D. Chidsey, P. C. McIntyre, *J. Electrochem. Soc.*, 2019, **166**, (14), H712
123. G. Papakonstantinou, I. Spanos, A. P. Dam, R. Schlögl, K. Sundmacher, *Phys. Chem. Chem. Phys.*, 2022, **24**, (23), 14579
124. X. Tan, J. Shen, N. Semagina, M. Secanell, *J. Catal.*, 2019, **371**, 57
125. Y.-R. Zheng, J. Vernieres, Z. Wang, K. Zhang, D. Hochfilzer, K. Krempl, T.-W. Liao, F. Presel, T. Altantzis, J. Fatermans, S. B. Scott, N. M. Secher, C. Moon, P. Liu, S. Bals, S. Van Aert, A. Cao, M. Anand, J. K. Nørskov, J. Kibsgaard, I. Chorkendorff, *Nat. Energy*, 2022, **7**, (1), 55
126. T. Malkow, G. De Marco, G. Tsotridis, "EU Harmonised Cyclic Voltammetry Test Method for Low Temperature Water Electrolysis Single Cells", JRC Validated Methods, Reference Methods and Measurement Report No. JRC111151, European Union, Petten, The Netherlands, 2018, 28 pp
127. T. Malkow, A. Pilenga, G. Tsotridis, "EU Harmonised Test Procedure: Electrochemical Impedance Spectroscopy for Water Electrolysis Cells", JRC Validated Methods, Reference Methods and Measurement Report No. JRC107053, European Union, Petten, The Netherlands, 2018, 33 pp

128. T. Malkow, A. Pilenga, G. Tsotridis, "EU Harmonised Polarisation Curve Test Method for Low Temperature Water Electrolysis", JRC Validated Methods, Reference Methods and Measurement Report No. JRC104045, European Union, Petten, The Netherlands, 2018, 48 pp
129. S. Siracusano, V. Baglio, S. A. Grigoriev, L. Merlo, V. N. Fateev, A. S. Aricò, *J. Power Sources*, 2017, **366**, 105
130. T. Reier, Z. Pawolek, S. Cherevko, M. Bruns, T. Jones, D. Teschner, S. Selve, A. Bergmann, H. N. Nong, R. Schlögl, K. J. J. Mayrhofer, P. Strasser, *J. Am. Chem. Soc.*, 2015, **137**, (40), 13031
131. V. Pfeifer, T. E. Jones, J. J. Velasco Vélez, C. Massué, R. Arrigo, D. Teschner, F. Girgsdies, M. Scherzer, M. T. Greiner, J. Allan, M. Hashagen, G. Weinberg, S. Piccinin, M. Hävecker, A. Knop-Gericke, R. Schlögl, *Surf. Interface Anal.*, 2015, **48**, (5), 261
132. C. Rozain, E. Mayousse, N. Guillet, P. Millet, *Appl. Catal. B: Environ.*, 2016, **182**, 153
133. M. Balcerzak, *Anal. Sci.*, 2002, **18**, (7), 737
134. S. Lee, X. Bi, R. B. Reed, J. F. Ranville, P. Herckes, P. Westerhoff, *Environ. Sci. Technol.*, 2014, **48**, (17), 10291
135. W. Sun, Z. Zhou, W. Q. Zaman, L. Cao, J. Yang, *ACS Appl. Mater. Interfaces*, 2017, **9**, (48), 41855
136. E. Willinger, C. Massué, R. Schlögl, M. G. Willinger, *J. Am. Chem. Soc.*, 2017, **139**, (34), 12093
137. J. Huang, S. B. Scott, I. Chorkendorff, Z. Wen, *ACS Catal.*, 2021, **11**, (20), 12745
138. S. B. Scott, R. R. Rao, C. Moon, J. E. Sørensen, J. Kibsgaard, Y. Shao-Horn, I. Chorkendorff, *Energy Environ. Sci.*, 2022, **15**, (5), 1977
139. L. Moriau, M. Smiljanić, A. Lončar, N. Hodnik, *ChemCatChem*, 2022, **14**, (20), e202200586
140. S. Abbou, R. Chattot, V. Martin, F. Claudel, L. Solà-Hernandez, C. Beauger, L. Dubau, F. Maillard, *ACS Catal.*, 2020, **10**, (13), 7283
141. H. Tang, S. Peikang, S. P. Jiang, F. Wang, M. Pan, *J. Power Sources*, 2007, **170**, (1), 85
142. M. Retuerto, L. Pascual, J. Torrero, M. A. Salam, Á. Tolosana-Moranchel, D. Gianolio, P. Ferrer, P. Kayser, V. Wilke, S. Stiber, V. Celorrio, M. Mokthar, D. G. Sanchez, A. S. Gago, K. A. Friedrich, M. A. Peña, J. A. Alonso, S. Rojas, *Nat. Commun.*, 2022, **13**, 7935
143. M. J. Burch, K. A. Lewinski, M. I. Buckett, S. Luopa, F. Sun, E. J. Olson, A. J. Steinbach, *J. Power Sources*, 2021, **500**, 229978
144. J. Murawski, S. B. Scott, R. Rao, K. Rigg, C. Zalitis, J. Stevens, J. Sharman, G. Hinds, I. E. L. Stephens, *Johnson Matthey Technol. Rev.*, 2024, **68**, (1), 147

The Authors

James Murawski graduated from the University of Southampton in 2018, UK, with a Master's degree in Chemistry. He is currently finishing PhD studies at Imperial College London in the area of acid based OER catalyst stability and degradation for PEM water electrolyser applications.

Soren B. Scott is a Danish-American researcher focused on electrocatalysis and its central role in the green transition. He has a PhD in Physics from the Technical University of Denmark and is presently a postdoctoral fellow based in Ifan Stephens' group at Imperial College London with funding from the Iberdrola Foundation's Energy for Future program.

Reshma R. Rao is a Royal Academy of Engineering Research Fellow in the Department of Materials, Imperial College London. Her research focuses on understanding reactivity at solid-liquid interfaces using *operando* spectroscopic techniques to design more active, stable and selective catalysts for electrochemical energy conversion technologies.

Katie Rigg graduated from the University of Leeds, UK, in 2018 with a MNatSci in Maths and Chemistry. She began her research at Johnson Matthey working on oxygen evolution and CO_2 reduction catalysis and now specialises in PEM water electrolysis focusing on CCM testing and anode layer characterisation.

Chris Zalitis is an electrochemistry group lead in the Hydrogen Technologies team at Johnson Matthey focusing on CCM development for hydrogen electrolysers. In 2008 he earned his Master of Chemistry degree at the University of Southampton and in 2012 he earned his PhD at Imperial College London on the topic of electrocatalysis of fuel cell reactions.

Jamie Stevens is water electrolysis research group leader at Johnson Matthey, Sonning Common, UK.

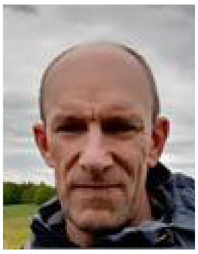

Jonathan Sharman runs the Hydrogen Technologies research groups at Johnson Matthey encompassing fuel cells, electrolysers and ion conducting membranes. His research interests cover the electrocatalysis within these systems, the structure-property relationships within CCMs and the electrochemical and *ex situ* characterisation techniques that probe the related material sets.

Gareth Hinds is NPL Fellow and Science Area Leader in the Electrochemistry Group at the National Physical Laboratory in Teddington, UK. His main research interests lie in the development of novel *in situ* diagnostic techniques and standard test methods for assessment of corrosion and material degradation in energy applications.

Ifan Stephens' research aims to enable the large-scale electrochemical conversion of renewable electricity and abundant feedstocks (H_2O, N_2, CO_2) to fuels and valuable chemicals (e.g. H_2, NH_3, C_2H_4). His focus is on catalysis. Stephens is the recipient of numerous awards, including the ERC Consolidator Grant, Clarivate Highly Cited Researcher, MIT's Peabody Visiting Associate Professorship and RSC's John Jeyes prize.